

Dynamical Scaling and Planckian Dissipation Due to Heavy-Fermion Quantum Criticality

Andreas Gleis^{1,2,*}, Seung-Sup B. Lee^{3,4,5,1,†}, Gabriel Kotliar^{2,6,‡} and Jan von Delft^{1,§}¹Arnold Sommerfeld Center for Theoretical Physics, Center for NanoScience, and Munich Center for Quantum Science and Technology, Ludwig-Maximilians-Universität München, 80333 Munich, Germany²Department of Physics and Astronomy, Rutgers University, Piscataway, New Jersey 08854, USA³Department of Physics and Astronomy, Seoul National University, Seoul 08826, Korea⁴Center for Theoretical Physics, Seoul National University, Seoul 08826, Korea⁵Institute for Data Innovation in Science, Seoul National University, Seoul 08826, Korea⁶Condensed Matter Physics and Materials Science Department, Brookhaven National Laboratory, Upton, New York 11973, USA

(Received 24 June 2024; accepted 23 January 2025; published 10 March 2025)

We study dynamical scaling associated with a Kondo-breakdown quantum-critical point (KB QCP) of the periodic Anderson model, treated by two-site cellular dynamical mean-field theory (2CDMFT). In the quantum-critical region, the dynamical staggered-spin susceptibility exhibits ω/T scaling. We propose a scaling ansatz that describes this behavior and reveals Planckian dissipation for the longest-lived excitations. The current susceptibility follows the same scaling, leading to strange-metal behavior for the optical conductivity and resistivity. Importantly, this behavior is driven by strong short-ranged vertex contributions, not single-particle decay. This suggests that the KB QCP described by 2CDMFT is a novel *intrinsic* (i.e., disorder-free) strange-metal fixed point. Our results for the optical conductivity match experimental observations on YbRh₂Si₂ and CeCoIn₅.

DOI: 10.1103/PhysRevLett.134.106501

Introduction—Strange metals [1–5], an enigmatic state of matter found in many strongly correlated materials [6–27], still defy a clear and unified understanding. Their phenomenology, including a low-temperature ($\gtrsim 10$ mK in YbRh₂Si₂ [28]) T -linear resistivity [9], an $\sim T \ln T$ specific heat and ω/T scaling [8,24,26,29–32], is incompatible with normal Fermi liquids [33]. Despite the ubiquity of strange metals, many basic questions remain unsettled [1], in particular, whether intrinsic strange metals, i.e., ones without disorder, exist [34,35].

Current attempts at explaining strange-metal phenomena often employ the marginal Fermi liquid (MFL) hypothesis [36], where electrons acquire a linear-in- T scattering rate due to scattering by a critical bosonic mode. However, it has recently been shown within the Yukawa-Sachdev-Ye-Kitaev (YSYK) approach that interaction disorder is required to also achieve a linear-in- T transport scattering rate [37,38]; i.e., the MFL strange metal is not intrinsic. The

same goes for MFL strange metals arising in single-site dynamical mean-field theory (DMFT) approaches [39], where single-electron and transport scattering rates coincide due to nonconserved momentum at the interaction vertex [40,41]. It is questionable whether the MFL approach can be reconciled with studies of disorder in cuprates [42], the fact that many strange metals are very clean [28,43] and with Hall angle measurements in strange metals [1,16,44–50].

In this Letter, we present a novel approach to intrinsic strange metals where phenomena like ω/T scaling and a linear-in- T resistivity arise from collective short-ranged fluctuations. The single-electron scattering rate does not play a direct role, in stark contrast to MFL approaches. We focus on heavy-fermion (HF) metals, where strange-metal behavior routinely emerges in the quantum-critical region of so-called Kondo breakdown (KB) quantum-critical points (QCPs) [51–56]. Previous studies have obtained interesting scaling behavior in the vicinity of a KB QCP [38,51,57–60], but apart from the MFL-based YSYK approach of Ref. [38], none of these studies explain the intriguing optical properties of HF strange metals.

We study the quantum-critical region of a KB QCP in the periodic Anderson model (PAM) described as a continuous orbital-selective Mott transition [56,61–64] via two-site cellular DMFT (2CDMFT) [41,65]. 2CDMFT maps the PAM to a self-consistent two-impurity Anderson model [56,61–64]. In a long companion paper [56], we

*Contact author: andreas.gleis@rutgers.edu

†Contact author: sslee@snu.ac.kr

‡Contact author: kotliar@physics.rutgers.edu

§Contact author: vondelft@lmu.de

used the numerical renormalization group (NRG) [66–71] as an impurity solver for 2CDMFT to identify a novel, 2CDMFT-stabilized KB QCP (by contrast, the Jones–Varma QCP is unstable [72–88]). We find ω/T scaling for several susceptibilities and strange-metal behavior for the optical conductivity and resistivity. Importantly, this behavior arises from dominant vertex contributions rather than single-particle decay.

Model and methods—We consider the PAM on a three-dimensional cubic lattice, involving an itinerant c band and a localized f band described by the Hamiltonian

$$H_{\text{PAM}} = \sum_{\mathbf{k}\sigma} (\epsilon_f - \mu) f_{\mathbf{k}\sigma}^\dagger f_{\mathbf{k}\sigma} + U \sum_i f_{i\uparrow}^\dagger f_{i\uparrow} f_{i\downarrow}^\dagger f_{i\downarrow} + V \sum_{\mathbf{k}\sigma} (c_{\mathbf{k}\sigma}^\dagger f_{\mathbf{k}\sigma} + \text{H.c.}) + \sum_{\mathbf{k}\sigma} (\epsilon_{c\mathbf{k}} - \mu) c_{\mathbf{k}\sigma}^\dagger c_{\mathbf{k}\sigma}. \quad (1)$$

Here, $f_{\mathbf{k}\sigma}^\dagger [c_{\mathbf{k}\sigma}^\dagger]$ creates a spin- σ f [c] electron with momentum \mathbf{k} , and $\epsilon_{c\mathbf{k}} = -2t \sum_{a=x,y,z} \cos(k_a)$ is the c -electron dispersion. We set the c -electron hopping $t = 1/6$ as an energy unit (half bandwidth = 1) and fix the f -orbital level $\epsilon_f = -5.5$, the interaction strength $U = 10$, and the chemical potential $\mu = 0.2$, as chosen in prior 2CDMFT studies [56,63,64]. The (T, V) phase diagram studied in detail in Ref. [56] (shown also in Ref. [89], Sec. S-I) is characterized by two V -dependent energy scales T_{FL} and T_{NFL} : The FL scale T_{FL} , below which FL behavior emerges, decreases toward and vanishes at the KB QCP at $V_c = 0.4575(25)$. This gives rise to a quantum-critical region between the scales $T_{\text{FL}} < T_{\text{NFL}}$, where we found non-Fermi liquid (NFL) behavior with strange-metal properties, such as a $T \ln T$ specific heat [56].

In this work, we study dynamical scaling and optical properties in the quantum-critical region. We fix $V = 0.46 \gtrsim V_c$ [96] and tune T . At $V = 0.46$, $T_{\text{NFL}}/T_{\text{FL}} > 10^3$; i.e., the NFL region extends over more than three decades, which allows us to study scaling. As in Ref. [56], we enforce U(1) charge and SU(2) spin symmetries (using the QSpace tensor library [97–99]), thereby excluding the possibility of symmetry breaking order by hand. We do not find tendencies toward symmetry breaking (divergent susceptibilities) for the parameters studied here.

Dynamical scaling—As a result of incomplete screening in the NFL region, many dynamical susceptibilities

$$\chi[\mathcal{A}, \mathcal{B}](\omega) = -i \int_0^\infty dt e^{i(\omega+i0^+)t} \langle [\mathcal{A}(t), \mathcal{B}^\dagger] \rangle \quad (2)$$

exhibit plateaus in their spectra $\chi''(\omega)$ at $T_{\text{FL}} < \omega < T_{\text{NFL}}$ and $T = 0$; cf. Ref. [56], Fig. 4. We use the shorthand $\chi[\mathcal{A}](\omega) = \chi[\mathcal{A}, \mathcal{A}](\omega)$ and $\chi(\omega) = \chi'(\omega) - i\pi\chi''(\omega)$. An example of a susceptibility governed by incomplete screening is $\chi[X^{xz}](\omega, T)$, where $X^{xz} = S_1^z - S_2^z$ is the staggered

f -electron spin on a two-site cluster. It exhibits ω/T scaling, as demonstrated in Fig. 1.

The T -dependent spectra $\chi''(\omega, T)$ and the corresponding real parts $\chi'(\omega, T)$ are shown in Figs. 1(a) and 1(b), respectively. As T is decreased from around T_{NFL} to T_{FL} , the aforementioned plateau in $\chi''(\omega, T)$ emerges between $T < \omega < T_{\text{NFL}}$, crossing over to $\propto \omega$ behavior for $\omega < T$. For $T < T_{\text{FL}}$, the spectrum becomes T independent. In the (imaginary) time domain, the plateau in χ'' implies SYK-like slow $1/\tau$ dynamics; see Fig. S1 of Ref. [89].

$\chi'(\omega, T)$ is related to $\chi''(\omega, T)$ via a Kramers-Kronig relation. It thus shows a logarithmic [100] ω dependence for $\max(T, T_{\text{FL}}) < \omega < T_{\text{NFL}}$ and is constant for $\omega < \max(T, T_{\text{FL}})$. As a result, $\chi'(0, T)$ [inset of Fig. 1] has a $\propto \ln T$ dependence for $T_{\text{FL}} < T < T_{\text{NFL}}$ and is constant for $T < T_{\text{FL}}$, where X^{xz} fluctuations are screened.

Figure 1(c) shows $\chi''(\omega, T)$ vs ω/T . In the NFL region ($T_{\text{FL}} < T < T_{\text{NFL}}$, $|\omega| < T_{\text{NFL}}$), the spectra all collapse onto a single curve. This demonstrates dynamical scaling in the sense that $T^\alpha \chi''(\omega, T) = \mathcal{X}''(\omega/T)$ with $\alpha = 0$. The real part [Fig. 1(d)] also shows ω/T scaling.

Scaling function and Planckian dissipation—In the NFL region ($T_{\text{FL}} < T < T_{\text{NFL}}$, $|\omega| < T_{\text{NFL}}$), the spectra of dynamical susceptibilities showing plateaus (e.g., $\chi[X^{xz}]$) can be fitted with a phenomenological ansatz for $\omega > 0$:

$$\tilde{\chi}''(\omega, T) = \chi_0 \int_T^{T_{\text{NFL}}} d\epsilon \frac{(1 - e^{-\frac{\omega}{\epsilon}}) (\frac{\epsilon}{T})^\nu bT}{\pi (\omega - a\epsilon)^2 + (bT)^2}. \quad (3)$$

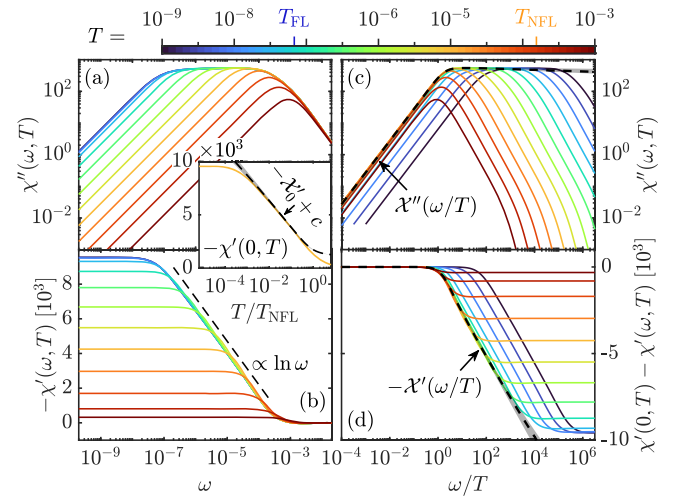


FIG. 1. Dynamical susceptibility $\chi[X^{xz}](\omega, T)$. (a) Spectral part and (b) corresponding real part for 13 choices of T (marked by ticks on the color bar). (c), (d) Scaling collapse of spectral and real parts. Black dashed lines show the universal scaling functions $\mathcal{X}''(\omega/T)$ and $\mathcal{X}'(\omega/T)$, respectively [cf. Eq. (4)]. Inset: $\chi'(0, T)$ (orange) and $\mathcal{X}'_0(T/T_{\text{NFL}}) + c$ [black dashed; cf. Eq. (4)]. The constant shift c accounts for spectral weight at $|\omega| > T_{\text{NFL}}$. Gray areas indicate fitting uncertainties [89].

$\omega < 0$ follows from antisymmetry of $\tilde{\chi}''$, and the real part $\tilde{\chi}'$ is determined through a Kramers-Kronig relation. χ_0, a, b , and ν are determined by fits to our spectra in the NFL region [89]. We find $a \simeq 10^{-1}$, $b \simeq 1$, and $\nu \simeq 0$; χ_0 determines the plateau value. (These parameters are V independent within our fitting accuracy.) When Eq. (3) is evaluated for $|\omega|, T \ll T_{\text{NFL}}$ one finds the scaling form

$$\tilde{\chi}(\omega, T) \simeq \mathcal{X}'_0 \left(\frac{T}{T_{\text{NFL}}} \right) + \mathcal{X}' \left(\frac{\omega}{T} \right) - i\pi \mathcal{X}'' \left(\frac{\omega}{T} \right). \quad (4)$$

An explicit T dependence, due to the high-energy cutoff T_{NFL} , only enters via $\mathcal{X}'_0(T/T_{\text{NFL}}) \simeq \tilde{\chi}'(0, T)$; otherwise, $\tilde{\chi}(\omega, T)$ only depends on the ratio ω/T (for more information on the universal scaling functions $\mathcal{X}'_0, \mathcal{X}'$, and \mathcal{X}'' , see Ref. [89]). In Figs. 1(c) and 1(d), we show that the scaling function \mathcal{X} captures $\chi[X^{xz}]$ well in the NFL region (black dashed lines).

The ansatz (3) is motivated by a fit of $\langle X^{xz}(t)X^{xz} \rangle$ to a superposition of coherent excitations with mean energy $a\epsilon$, decay rate bT , and density of states $(\epsilon/T)^\nu$ [89]. Since $b \simeq 1$, these coherent excitations have a decay rate $\gamma \simeq T$ or correspondingly a lifetime $\tau \simeq 1/T$; i.e., the longest-lived X^{xz} excitations have a Planckian lifetime.

Optical conductivity—Our 2CDMFT approximation allows us to compute the *local* current susceptibility $\chi[j_i^a](\omega, T)$ of the lattice model from the effective impurity model. Here, $j_i^a = -ite \sum_{\sigma} (c_{i\sigma}^\dagger c_{i+a\sigma} - c_{i+a\sigma}^\dagger c_{i\sigma})$ is the current operator in the a direction, with i and $i + \mathbf{a}$ nearest neighbors on the lattice, chosen to also correspond to the two sites of the self-consistent impurity model.

For optical experiments and electronic transport, the uniform current susceptibility $\chi[j_{\mathbf{q}=\mathbf{0}}^a](\omega, T)$ is relevant, where $j_{\mathbf{q}}^a$ is the \mathbf{q} -dependent current in the a direction $j_{\mathbf{q}}^a = (1/N) \sum_{i\sigma} e^{-i\mathbf{q}\cdot\mathbf{r}_i} j_i^a$. Assuming translation symmetry, $\chi[j_{\mathbf{0}}^a]$ can be expressed as a sum $\chi[j_i^a] + \chi_{\text{nl}}[j]$ of local and nonlocal parts, with $\chi_{\text{nl}}[j] = (1/N) \sum_{\ell \neq i} \chi[j_\ell^a, j_i^a] = \chi[j_{\mathbf{0}}^a] - \chi[j_i^a]$. The computation of $\chi_{\text{nl}}[j]$ would require four-point correlators [101–103] for the self-consistent two-impurity model, which currently exceeds our computational resources. Hence, we approximate it by its bubble contribution $\chi_{\text{nl,B}}[j] = \chi_{\text{B}}[j_{\mathbf{0}}^a] - \chi_{\text{B}}[j_i^a]$. Thus, we use

$$\chi[j_{\mathbf{0}}^a] \approx \chi[j_i^a] + \chi_{\text{nl,B}}[j] = \chi_{\text{B}}[j_{\mathbf{0}}^a] + \chi_{\text{vtx}}[j_i^a], \quad (5)$$

where $\chi_{\text{vtx}}[j_i^a] = \chi[j_i^a] - \chi_{\text{B}}[j_i^a]$ is the *vertex* contribution to the local current susceptibility.

The uniform current spectrum determines the real part of the optical conductivity $\sigma'(\omega, T) = (\pi/\omega) \chi''[j_{\mathbf{0}}^a](\omega, T)$ shown in Fig. 2(a). At $T \ll T_{\text{FL}}$ (blue and black), it features a hybridization gap around $\omega \simeq T_{\text{NFL}}$, ω^{-1} behavior for $T_{\text{FL}} < \omega < T_{\text{NFL}}$, and a Drude peak at low frequencies below T_{FL} . These features emerge as the temperature is lowered from $T \gg T_{\text{NFL}}$: The hybridization gap forms

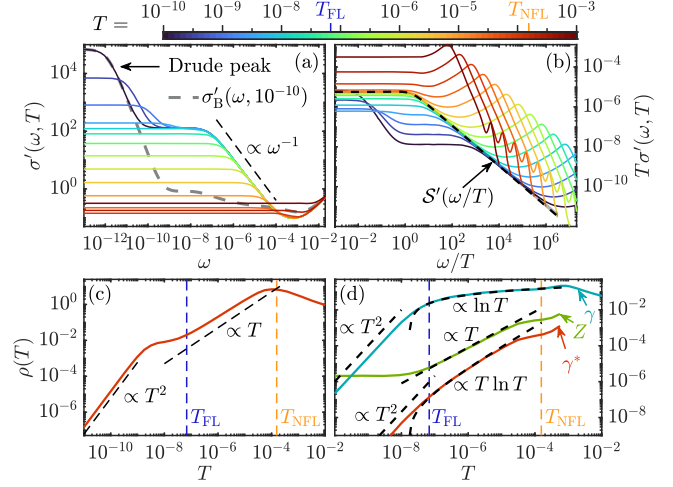


FIG. 2. (a) Real part of the optical conductivity $\sigma'(\omega, T)$; gray dashed line, bubble contribution at $T = 10^{-10}$. (b) ω/T scaling of $T\sigma'(\omega, T)$; black dashed line, the scaling function S' of Eq. (6). (c) The resistivity $\rho(T)$. (d) The single-particle decay rate γ^* , quasiparticle (QP) weight Z , and QP decay rate γ^* .

around $T \simeq T_{\text{NFL}}$ (red), the ω^{-1} feature emerges between $T_{\text{FL}} < T < T_{\text{NFL}}$ (yellow and green), and the Drude peak finally emerges for $T < T_{\text{FL}}$ (blue and black).

The ω^{-1} feature in the NFL region is due to ω/T scaling of $\chi''[j_i^a]$ (Fig. S5 in Ref. [89]) similar to that of $\chi''[X^{xz}]$. Remarkably, $\chi''[j_i^a]$, just as $\chi''[X^{xz}]$, is well described by the ansatz (3) (see Fig. S8 of Ref. [89]), implying ω/T scaling and Planckian dissipation of current fluctuations. In the NFL region, $T_{\text{FL}} < T < T_{\text{NFL}}$, $\sigma'(\omega, T)$ is therefore governed by a scaling function S' :

$$T\sigma'(\omega, T) = (T/\omega)\pi\mathcal{X}''(\omega/T) = S'(\omega/T). \quad (6)$$

Figure 2(b) shows that $T\sigma'(\omega, T)$ is indeed well described by this scaling function (black dashed line). Similarly, we find that $T\sigma''(\omega, T) = S''(\omega/T)$, with $S''(x) = \mathcal{X}'(x)/x$; see Ref. [89], Secs. S–V, Fig. S10.

The scaling behavior (6) has two striking implications for the NFL region $T_{\text{FL}} < T < T_{\text{NFL}}$: First, a scaling collapse is achieved for $T^\alpha \sigma'(\omega, T)$ with $\alpha = 1$, an exponent which was also found experimentally [24,26,32]. Second, the static conductivity $\sigma(T) = \sigma'(0, T) = S'(0)/T$ scales as $1/T$, implying T -linear behavior for the resistivity, $\rho(T) = 1/\sigma(T) \propto T$. This is borne out in Fig. 2(c): $\rho(T)$ has a maximum around T_{NFL} , where the hybridization gap forms, then decreases $\propto T$ for $T_{\text{FL}} < T < T_{\text{NFL}}$, before finally becoming $\propto T^2$ below T_{FL} .

The ω/T scaling and linear-in- T resistivity in the NFL region is completely dominated by the vertex contribution to the current susceptibility $\chi''_{\text{vtx}}[j_i^a] \gg |\chi''_{\text{B}}[j_{\mathbf{0}}^a]|$. To visualize this, we have included the bubble contribution $\sigma'_B(\omega)$ (gray dashed) at $T = 10^{-10}$ in Fig. 2(a). In the NFL region ($T_{\text{FL}} < |\omega| < T_{\text{NFL}}$), σ'_B is orders of magnitude smaller

than $\sigma'(\omega)$ and, crucially, does not show ω^{-1} behavior. Also, $\sigma'_B(\omega, T)$ does not exhibit ω/T scaling. However, it contributes the Drude peak at $|\omega|, T < T_{\text{FL}}$.

Next, we consider the single-particle decay rate γ [104], QP weight Z , and QP decay rate γ^* ,

$$\gamma = \text{Im}G_{\mathbf{k}_F}^{-1}(0), \quad Z^{-1} = \partial_\omega \text{Re}G_{\mathbf{k}_F}^{-1}(0), \quad \gamma^* = Z\gamma \quad (7)$$

shown in Fig. 2(d). Z and γ^* determine the weight and width of the Lorentzian line shape in the single-particle spectral function at \mathbf{k}_F , while γ governs the bubble contribution to the conductivity $\sigma'_B \propto 1/\gamma$. In the NFL region, we find $\gamma \propto \ln T$, i.e., $\sigma'_B \propto 1/\ln T \ll \sigma' \propto 1/T$. Thus, the conductivity in the NFL region is not governed by single-particle decay but by short-ranged collective current fluctuations, in contrast to the MFL paradigm.

In the FL region, $\gamma, \gamma^* \propto T^2$, and $Z = \text{const}$ [Fig. 2(d)] as expected, leading to a Drude peak of width $\propto T^2$ and $\rho(T) \propto T^2$; i.e., these features are due to long-lived coherent QP carrying the current. Since we neglect *non-local* vertex contributions which encode momentum conservation during small-momentum scattering [105], the transport relaxation rate, and thus the T^2 prefactor of $\rho(T)$, is set purely by the QP decay rate and is therefore very likely overestimated.

Optical mass and transport scattering rate—To obtain additional insights, we determined the transport scattering rate $\tau^{-1}(\omega)$ and the optical mass $m^*(\omega)$ defined as

$$\tau^{-1}(\omega) = \text{Re}\sigma^{-1}(\omega), \quad m^*(\omega) = -\omega^{-1}\text{Im}\sigma^{-1}(\omega) \quad (8)$$

following Ref. [106], Eq. (1). Here, $\sigma(\omega)$ is the complex optical conductivity, and we omitted constant prefactors to focus on qualitative features.

Figure 3(a) shows our results for $\tau^{-1}(\omega)$, with $\tau^{-1}(0) = \tau_0^{-1} = \rho(T) \propto T$ for $T_{\text{FL}} < T < T_{\text{NFL}}$. For $\max(T_{\text{FL}}, T) < |\omega| < T_{\text{NFL}}$, $\tau^{-1}(\omega)$ has a nontrivial ω and T dependence, not following a simple power law with possible logarithmic corrections. There, $\sigma(\omega)$ does not fit a Drude form. Non-Drude behavior is most clearly visible from $\sigma'(\omega, T)$ [cf. Fig. 2(a)], which shows a ω^{-1} dependence in the NFL region, whereas a usual Drude peak would imply an ω^{-2} dependence. Similar non-Drude behavior of the optical conductivity has been observed in YbRh_2Si_2 [24,26].

Remarkably, in the NFL region ($T_{\text{FL}} < T < T_{\text{NFL}}$) at low frequencies $|\omega| \lesssim T$, $\tau^{-1}(\omega)$ shows a quadratic frequency dependence $\tau^{-1}(\omega) - \tau_0^{-1} \sim c(T)\omega^2$; cf. Fig. 3(c). An ω^2 dependence of $\tau^{-1}(\omega)$ was also found in CeCoIn_5 ; cf. Figs. 4(a) and 4(c) of Ref. [106] and its discussion. However, whereas for an FL the prefactor $c(T)$ does not depend on the temperature, the ω/T scaling of $\sigma(\omega, T)$ in the strange-metal region implies $c(T) \sim 1/T$; see Ref. [89], Sec. S–V.

We emphasize that in our results, $\tau^{-1}(\omega)$ is not proportional to $-\text{Im}\Sigma(\omega)$ (without vertex contributions, a

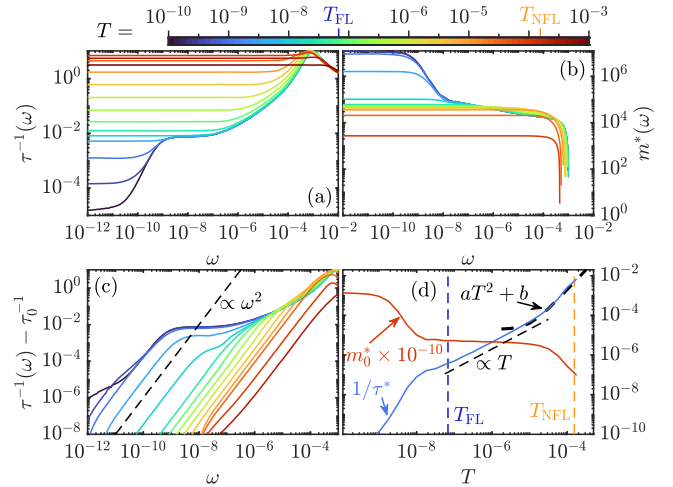


FIG. 3. Frequency dependence of (a) the transport scattering rate $\tau^{-1}(\omega)$, (b) the effective mass $m^*(\omega)$, and (c) $\tau^{-1}(\omega) - \tau_0^{-1}$, where $\tau_0^{-1} = \tau^{-1}(0) = \rho$. (d) Temperature dependence of $\tau^{*-1} = \tau_0^{-1}/m_0^*$ and $m_0^* = m^*(0)$.

proportionality would be expected). In our 2CDMFT + NRG approach to the PAM, $-\text{Im}\Sigma(\omega)$ has a logarithmic ω and T dependence; cf. Figs. 11 and 12 of Ref. [56]. The ω and T dependence $\tau^{-1}(\omega)$ discussed above differs from that, again illustrating the importance of vertex contributions.

Figure 3(b) shows $m^*(\omega)$. In the NFL region ($T_{\text{FL}} < T < T_{\text{NFL}}$), $m^*(\omega)$ is strongly frequency dependent around the NFL scale $\omega \simeq 10^{-3} - 10^{-4} \simeq T_{\text{NFL}}$, and then saturates to an almost ω - and T -independent value $m^*(\omega) \simeq m^*(0) = m_0^*$. The weak ω and T dependence of $m^*(\omega)$ does not seem to follow a simple power law. Interestingly, even though there are no well-defined QPs in the strange-metal region, there nevertheless seems to be a somewhat well-defined effective mass m_0^* . We emphasize though that in the NFL region, $m_0^* \simeq 5 \times 10^4 \sim 10/T_{\text{NFL}}$ is orders of magnitude smaller than in the FL region, where $m_0^* \simeq 1.5 \times 10^7 \sim 1/T_{\text{FL}}$; cf. Fig. 3(d). The effective mass in the NFL region is therefore decisively distinct from the QP mass in the low-temperature FL region.

In Fig. 3(d), we show the temperature dependence of the renormalized scattering rate $\tau^{*-1} = \tau_0^{-1}/m_0^*$ (blue), together with m_0^* (red). Deep in the NFL region, we find $\tau^{*-1} \sim T$, since $\tau_0^{-1} \sim T$ and $m_0^* = \text{const}$. Interestingly, in the crossover region between $T \simeq T_{\text{NFL}}$ and $T \simeq 10^{-1}T_{\text{NFL}}$, τ^{*-1} deviates from the linear-in- T behavior and is consistent with FL-like T^2 behavior.

A similar T^2 behavior was reported for CeCoIn_5 in Ref. [106], where this behavior was interpreted as evidence for a hidden Fermi liquid. Our calculations suggest that the T^2 behavior is rather a crossover behavior, and measurements at lower temperatures are necessary for a definite conclusion. Such measurements are presumably not possible in CeCoIn_5 due to its relatively high T_c . A promising candidate material to clarify whether $\tau^{*-1} \sim T$ or $\sim T^2$ may

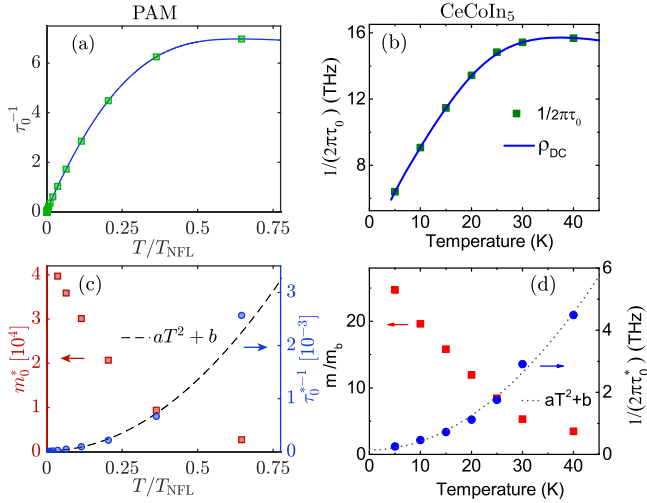


FIG. 4. (a) Scattering rate $\tau_0^{-1} = \rho(T)$ for $T \lesssim T_{\text{NFL}}$ for the PAM. Green squares, data points; blue line, guide to the eye. (b) τ_0^{-1} (green squares) and rescaled resistivity (blue line) for CeCoIn₅ close to its coherence temperature $T^* = 40$ K, adapted from Fig. 4(b) of Ref. [106]. (c) Renormalized scattering rate τ_0^{*-1} (blue circles) and effective mass m_0^* (red squares) for the PAM. (d) τ_0^{*-1} (blue circles) and m_0^* (red squares) for CeCoIn₅, adapted from Fig. 4(d) of Ref. [106].

be YbRh₂Si₂. To emphasize the similarity between the experimental data on CeCoIn₅ and our results on the PAM more visually, we show the resistivity $\rho(T)$ of the PAM in Fig. 4(a) on a linear scale in the crossover region, next to the corresponding experimental data on CeCoIn₅ [Fig. 4(b)], adapted from Fig. 4(b) of Ref. [106]. In Figs. 4(c) and 4(d), we further show the data for the renormalized scattering rate and the effective mass for both the PAM and CeCoIn₅, respectively [adapted from Fig. 4(d) of Ref. [106] for the latter]. The experimental data on CeCoIn₅ and our numerical data on the PAM show remarkable qualitative agreement in the crossover region: (i) The resistivity has a broad maximum and turns to linear in T , (ii) the renormalized scattering rate $\tau^{*-1} \propto T^2$, and (iii) the effective mass m_0^* increases with the temperature in a remarkably similar fashion. An estimate of the suitability of our model parameters for CeCoIn₅ is provided in Ref. [89]. A more detailed quantitative description of CeCoIn₅ (or YbRh₂Si₂) will require a more realistic future study, e.g., using LDA + DMFT + NRG.

Discussion and outlook—Our work provides a promising route toward an intrinsic strange metal. However, we have not yet achieved a full understanding of the current decay mechanism. An inherent feature of (C)DMFT is that the interaction vertex does not ensure conservation of crystal momentum [40,41]. Therefore, electron-electron scattering does not conserve crystal momentum, leading to current decay. This mechanism usually manifests as a dominant bubble contribution (in single-site DMFT, this is the only contribution). A dominant bubble contribution is also key

to the YSYK approach [37] to strange metals. There, a disordered Yukawa coupling leads to nonconserved momentum in scattering processes. The result is an MFL where strange-metal scaling arises in the bubble contribution, and interaction disorder is needed to avoid its cancellation by the vertex contribution. By contrast, in our 2CDMFT approach, the strange-metal scaling in the NFL region arises *entirely from the vertex contribution*, and not at all from the (much smaller) bubble contribution. This strongly suggests that the current decay mechanism is not due to the nonconservation of crystal momentum at the interaction vertex. Our 2CDMFT approach also includes crystal momentum conserving umklapp scattering processes between momenta around $\mathbf{k} = (0, 0, 0)$ and $\mathbf{k} = (\pi, \pi, \pi)$ which flip the current. We conjecture that these cause our observed strange-metal scaling, but leave a detailed analysis for future work.

Acknowledgments—We thank Assa Auerbach, Silke Bühler-Paschen, Andrey Chubukov, Piers Coleman, Dominic Else, Fabian Kugler, Antoine Georges, Sean Hartnoll, Andy Millis, Achim Rosch, Subir Sachdev, Qimiao Si, Katharina Stadler, Senthil Todadri, Matthias Vojta, Andreas Weichselbaum, and Krzysztof Wójcik for helpful discussions. This work was funded in part by the Deutsche Forschungsgemeinschaft under Germany’s Excellence Strategy EXC-2111 (Project No. 390814868). It is part of the Munich Quantum Valley supported by the Bavarian state government with funds from the Hightech Agenda Bayern Plus. This work was further supported by Grants No. INST 86/1885-1 FUGG and No. LE 3883/2-2 of the German Research Foundation. S. S. B. L. was supported by Samsung Electronics Co., Ltd. (Grant No. IO220817-02066-01), the Global-LAMP Program of the National Research Foundation of Korea (NRF) grant funded by the Ministry of Education (Grant No. RS-2023-00301976), the NRF grant funded by the Korean government (MSIT) (Grant No. RS-2023-00214464), and the NRF grant funded by the Korean government (MEST) (Grant No. 2019R1A6A1A10073437). The National Science Foundation supported G.K. under Grant No. DMR-1733071, and J. v. D. in part under Grant No. PHY-1748958. A.G. acknowledges support from the Abrahams Postdoctoral Fellowship of the Center for Materials Theory at Rutgers University.

- [1] P. W. Phillips, N. E. Hussey, and P. Abbamonte, Stranger than metals, *Science* **377**, eabh4273 (2022).
- [2] S. A. Hartnoll and A. P. Mackenzie, Colloquium: Planckian dissipation in metals, *Rev. Mod. Phys.* **94**, 041002 (2022).
- [3] D. Chowdhury, A. Georges, O. Parcollet, and S. Sachdev, Sachdev-Ye-Kitaev models and beyond: Window into non-Fermi liquids, *Rev. Mod. Phys.* **94**, 035004 (2022).

- [4] J. Zaanen, Why the temperature is high, *Nature (London)* **430**, 512 (2004).
- [5] J. G. Checkelsky, B. A. Bernevig, P. Coleman, Q. Si, and S. Paschen, Flat bands, strange metals and the Kondo effect, *Nat. Rev. Mater.* **9**, 509 (2024).
- [6] B. Keimer, S. A. Kivelson, M. R. Norman, S. Uchida, and J. Zaanen, From quantum matter to high-temperature superconductivity in copper oxides, *Nature (London)* **518**, 179 (2015).
- [7] B. Michon, C. Girod, S. Badoux, J. Kačmarčík, Q. Ma, M. Dragomir, H. A. Dabkowska, B. D. Gaulin, J.-S. Zhou, S. Pyon, T. Takayama, H. Takagi, S. Verret, N. Doiron-Leyraud, C. Marcenat, L. Taillefer, and T. Klein, Thermodynamic signatures of quantum criticality in cuprate superconductors, *Nature (London)* **567**, 218 (2019).
- [8] B. Michon, C. Berthod, C. W. Rischau, A. Ataei, L. Chen, S. Komiyama, S. Ono, L. Taillefer, D. van der Marel, and A. Georges, Reconciling scaling of the optical conductivity of cuprate superconductors with Planckian resistivity and specific heat, *Nat. Commun.* **14**, 3033 (2023).
- [9] A. Legros, S. Benhabib, W. Tabis, F. Laliberté, M. Dion, M. Lizaire, B. Vignolle, D. Vignolles, H. Raffy, Z. Z. Li, P. Auban-Senzier, N. Doiron-Leyraud, P. Fournier, D. Colson, L. Taillefer, and C. Proust, Universal T -linear resistivity and Planckian dissipation in overdoped cuprates, *Nat. Phys.* **15**, 142 (2019).
- [10] S. Kasahara, T. Shibauchi, K. Hashimoto, K. Ikada, S. Tonegawa, R. Okazaki, H. Shishido, H. Ikeda, H. Takeya, K. Hirata, T. Terashima, and Y. Matsuda, Evolution from non-Fermi- to Fermi-liquid transport via isovalent doping in $\text{BaFe}_2(\text{As}_{1-x}\text{P}_x)_2$ superconductors, *Phys. Rev. B* **81**, 184519 (2010).
- [11] E. Abrahams and Q. Si, Quantum criticality in the iron pnictides and chalcogenides, *J. Phys. Condens. Matter* **23**, 223201 (2011).
- [12] A. Chubukov and P. J. Hirschfeld, Iron-based superconductors, seven years later, *Phys. Today* **68**, No. 6, 46 (2015).
- [13] Q. Si and N. E. Hussey, Iron-based superconductors: Teenage, complex, challenging, *Phys. Today* **76**, No. 5, 34 (2023).
- [14] J. G. Analytis, H.-H. Kuo, R. D. McDonald, M. Wartenbe, P. M. C. Rourke, N. E. Hussey, and I. R. Fisher, Transport near a quantum critical point in $\text{BaFe}_2(\text{As}_{1-x}\text{P}_x)_2$, *Nat. Phys.* **10**, 194 (2014).
- [15] I. M. Hayes, R. D. McDonald, N. P. Breznay, T. Helm, P. J. W. Moll, M. Wartenbe, A. Shekhter, and J. G. Analytis, Scaling between magnetic field and temperature in the high-temperature superconductor $\text{BaFe}_2(\text{As}_{1-x}\text{P}_x)_2$, *Nat. Phys.* **12**, 916 (2016).
- [16] W. K. Huang, S. Hosoi, M. Čulo, S. Kasahara, Y. Sato, K. Matsuura, Y. Mizukami, M. Berben, N. E. Hussey, H. Kontani, T. Shibauchi, and Y. Matsuda, Non-fermi liquid transport in the vicinity of the nematic quantum critical point of superconducting $\text{FeSe}_{1-x}\text{S}_x$, *Phys. Rev. Res.* **2**, 033367 (2020).
- [17] X. Jiang, M. Qin, X. Wei, L. Xu, J. Ke, H. Zhu, R. Zhang, Z. Zhao, Q. Liang, Z. Wei, Z. Lin, Z. Feng, F. Chen, P. Xiong, J. Yuan, B. Zhu, Y. Li, C. Xi, Z. Wang, M. Yang, J. Wang, T. Xiang, J. Hu, K. Jiang, Q. Chen, K. Jin, and Z. Zhao, Interplay between superconductivity and the strange-metal state in FeSe, *Nat. Phys.* **19**, 365 (2023).
- [18] Y. Cao, V. Fatemi, S. Fang, K. Watanabe, T. Taniguchi, E. Kaxiras, and P. Jarillo-Herrero, Unconventional superconductivity in magic-angle graphene superlattices, *Nature (London)* **556**, 43 (2018).
- [19] Y. Cao, D. Chowdhury, D. Rodan-Legrain, O. Rubies-Bigorda, K. Watanabe, T. Taniguchi, T. Senthil, and P. Jarillo-Herrero, Strange metal in magic-angle graphene with near Planckian dissipation, *Phys. Rev. Lett.* **124**, 076801 (2020).
- [20] A. Jaoui, I. Das, G. Di Battista, J. Díez-Mérida, X. Lu, K. Watanabe, T. Taniguchi, H. Ishizuka, L. Levitov, and D. K. Efetov, Quantum critical behaviour in magic-angle twisted bilayer graphene, *Nat. Phys.* **18**, 633 (2022).
- [21] H. von Löhneysen, Non-Fermi-liquid behaviour in the heavy-fermion system $\text{CeCu}_{6-x}\text{Au}_x$, *J. Phys. Condens. Matter* **8**, 9689 (1996).
- [22] O. Trovarelli, C. Geibel, S. Mederle, C. Langhammer, F. M. Grosche, P. Gegenwart, M. Lang, G. Sporn, and F. Steglich, YbRh_2Si_2 : Pronounced non-Fermi-liquid effects above a low-lying magnetic phase transition, *Phys. Rev. Lett.* **85**, 626 (2000).
- [23] J. Paglione, M. A. Tanatar, D. G. Hawthorn, E. Boaknin, R. W. Hill, F. Ronning, M. Sutherland, L. Taillefer, C. Petrovic, and P. C. Canfield, Field-induced quantum critical point in CeCoIn_5 , *Phys. Rev. Lett.* **91**, 246405 (2003).
- [24] L. Prochaska, X. Li, D. C. MacFarland, A. M. Andrews, M. Bonta, E. F. Bianco, S. Yazdi, W. Schrenk, H. Detz, A. Limbeck, Q. Si, E. Ringe, G. Strasser, J. Kono, and S. Paschen, Singular charge fluctuations at a magnetic quantum critical point, *Science* **367**, 285 (2020).
- [25] M. Taupin and S. Paschen, Are heavy fermion strange metals Planckian?, *Crystals* **12**, 251 (2022).
- [26] X. Li, J. Kono, Q. Si, and S. Paschen, Is the optical conductivity of heavy fermion strange metals Planckian?, *Front. Electron. Mater.* **2**, 934691 (2023).
- [27] L. Chen, D. T. Lowder, E. Bakali, A. M. Andrews, W. Schrenk, M. Waas, R. Svagera, G. Eguchi, L. Prochaska, Y. Wang, C. Setty, S. Sur, Q. Si, S. Paschen, and D. Natelson, Shot noise in a strange metal, *Science* **382**, 907 (2023).
- [28] D. H. Nguyen, A. Sidorenko, M. Taupin, G. Knebel, G. Lapertot, E. Schuberth, and S. Paschen, Superconductivity in an extreme strange metal, *Nat. Commun.* **12**, 4341 (2021).
- [29] M. C. Aronson, R. Osborn, R. A. Robinson, J. W. Lynn, R. Chau, C. L. Seaman, and M. B. Maple, Non-Fermi-liquid scaling of the magnetic response in $\text{UCu}_{5-x}\text{Pd}_x$ ($x = 1, 1.5$), *Phys. Rev. Lett.* **75**, 725 (1995).
- [30] A. Schröder, G. Aeppli, R. Coldea, M. Adams, O. Stockert, H. Löhneysen, E. Bucher, R. Ramazashvili, and P. Coleman, Onset of antiferromagnetism in heavy-fermion metals, *Nature (London)* **407**, 351 (2000).
- [31] L. Poudel, J. M. Lawrence, L. S. Wu, G. Ehlers, Y. Qiu, A. F. May, F. Ronning, M. D. Lumsden, D. Mandrus, and A. D. Christianson, Multicomponent fluctuation spectrum at the quantum critical point in $\text{CeCu}_{6-x}\text{Ag}_x$, *npj Quantum Mater.* **4**, 52 (2019).

- [32] C.-J. Yang, S. Pal, F. Zamani, K. Kliemt, C. Krellner, O. Stockert, H. v. Löhneysen, J. Kroha, and M. Fiebig, Terahertz conductivity of heavy-fermion systems from time-resolved spectroscopy, *Phys. Rev. Res.* **2**, 033296 (2020).
- [33] G. Giuliani and G. Vignale, *Quantum Theory of the Electron Liquid* (Cambridge University Press, Cambridge, England, 2005), 10.1017/CBO9780511619915.
- [34] D. V. Else, R. Thorngren, and T. Senthil, Non-Fermi liquids as ersatz Fermi liquids: General constraints on compressible metals, *Phys. Rev. X* **11**, 021005 (2021).
- [35] D. V. Else and T. Senthil, Strange metals as ersatz Fermi liquids, *Phys. Rev. Lett.* **127**, 086601 (2021).
- [36] C. M. Varma, P. B. Littlewood, S. Schmitt-Rink, E. Abrahams, and A. E. Ruckenstein, Phenomenology of the normal state of Cu-O high-temperature superconductors, *Phys. Rev. Lett.* **63**, 1996 (1989).
- [37] A. A. Patel, H. Guo, I. Esterlis, and S. Sachdev, Universal theory of strange metals from spatially random interactions, *Science* **381**, 790 (2023).
- [38] E. E. Aldape, T. Cookmeyer, A. A. Patel, and E. Altman, Solvable theory of a strange metal at the breakdown of a heavy Fermi liquid, *Phys. Rev. B* **105**, 235111 (2022).
- [39] P. Cha, N. Wentzell, O. Parcollet, A. Georges, and E.-A. Kim, Linear resistivity and Sachdev-Ye-Kitaev (SYK) spin liquid behavior in a quantum critical metal with spin-1/2 fermions, *Proc. Natl. Acad. Sci. U.S.A.* **117**, 18341 (2020).
- [40] A. Georges, G. Kotliar, W. Krauth, and M. J. Rozenberg, Dynamical mean-field theory of strongly correlated fermion systems and the limit of infinite dimensions, *Rev. Mod. Phys.* **68**, 13 (1996).
- [41] T. A. Maier, M. Jarrell, T. Pruschke, and M. Hettler, Quantum cluster theories, *Rev. Mod. Phys.* **77**, 1027 (2005).
- [42] F. Rullier-Albenque, P. A. Vieillefond, H. Alloul, A. W. Tyler, P. Lejay, and J. F. Marucco, Universal T_c depression by irradiation defects in underdoped and overdoped cuprates?, *Europhys. Lett.* **50**, 81 (2000).
- [43] M. A. Tanatar, J. Paglione, C. Petrovic, and L. Taillefer, Anisotropic violation of the Wiedemann-Franz law at a quantum critical point, *Science* **316**, 1320 (2007).
- [44] T. R. Chien, Z. Z. Wang, and N. P. Ong, Effect of Zn impurities on the normal-state Hall angle in single-crystal $\text{YBa}_2\text{Cu}_{3-x}\text{Zn}_x\text{O}_{7-\delta}$, *Phys. Rev. Lett.* **67**, 2088 (1991).
- [45] A. Carrington, A. P. Mackenzie, C. T. Lin, and J. R. Cooper, Temperature dependence of the Hall angle in single-crystal $\text{YBa}_2(\text{Cu}_{1-x}\text{Co}_x)_3\text{O}_{7-\delta}$, *Phys. Rev. Lett.* **69**, 2855 (1992).
- [46] S. Paschen, T. Lühmann, S. Wirth, P. Gegenwart, O. Trovarelli, C. Geibel, F. Steglich, P. Coleman, and Q. Si, Hall-effect evolution across a heavy-fermion quantum critical point, *Nature (London)* **432**, 881 (2004).
- [47] Y. Nakajima, K. Izawa, Y. Matsuda, S. Uji, T. Terashima, H. Shishido, R. Settai, Y. Onuki, and H. Kontani, Normal-state Hall angle and magnetoresistance in quasi-2d heavy fermion CeCoIn_5 near a quantum critical point, *J. Phys. Soc. Jpn.* **73**, 5 (2004).
- [48] Y. Nakajima, H. Shishido, H. Nakai, T. Shibauchi, K. Behnia, K. Izawa, M. Hedo, Y. Uwatoko, T. Matsumoto, R. Settai, Y. Onuki, H. Kontani, and Y. Matsuda, Non-Fermi liquid behavior in the magnetotransport of CeMIn_5 (M: Co and Rh): Striking similarity between quasi two-dimensional heavy fermion and high- T_c cuprates, *J. Phys. Soc. Jpn.* **76**, 024703 (2007).
- [49] M. Čulo, M. Berben, Y.-T. Hsu, J. Ayres, R. D. H. Hinlopen, S. Kasahara, Y. Matsuda, T. Shibauchi, and N. E. Hussey, Putative Hall response of the strange metal component in $\text{FeSe}_{1-x}\text{S}_x$, *Phys. Rev. Res.* **3**, 023069 (2021).
- [50] R. Lyu, Z. Tuchfeld, N. Verma, H. Tian, K. Watanabe, T. Taniguchi, C. N. Lau, M. Randeria, and M. Bockrath, Strange metal behavior of the Hall angle in twisted bilayer graphene, *Phys. Rev. B* **103**, 245424 (2021).
- [51] Q. Si, S. Rabello, K. Ingersent, and J. L. Smith, Locally critical quantum phase transitions in strongly correlated metals, *Nature (London)* **413**, 804 (2001).
- [52] P. Coleman, C. Pépin, Q. Si, and R. Ramazashvili, How do Fermi liquids get heavy and die?, *J. Phys. Condens. Matter* **13**, R723 (2001).
- [53] P. Coleman and C. Pépin, What is the fate of the heavy electron at a quantum critical point?, *Physica (Amsterdam)* **312–313B**, 383 (2002).
- [54] T. Senthil, S. Sachdev, and M. Vojta, Fractionalized Fermi liquids, *Phys. Rev. Lett.* **90**, 216403 (2003).
- [55] T. Senthil, M. Vojta, and S. Sachdev, Weak magnetism and non-Fermi liquids near heavy-fermion critical points, *Phys. Rev. B* **69**, 035111 (2004).
- [56] A. Gleis, S.-S. B. Lee, G. Kotliar, and J. von Delft, Emergent properties of the periodic Anderson model: A high-resolution, real-frequency study of heavy-fermion quantum criticality, *Phys. Rev. X* **14**, 041036 (2024).
- [57] L. Zhu, S. Kirchner, Q. Si, and A. Georges, Quantum critical properties of the Bose-Fermi Kondo model in a large- N limit, *Phys. Rev. Lett.* **93**, 267201 (2004).
- [58] M. T. Glossop, S. Kirchner, J. H. Pixley, and Q. Si, Critical Kondo destruction in a pseudogap Anderson model: Scaling and relaxational dynamics, *Phys. Rev. Lett.* **107**, 076404 (2011).
- [59] A. Cai, Z. Yu, H. Hu, S. Kirchner, and Q. Si, Dynamical scaling of charge and spin responses at a Kondo destruction quantum critical point, *Phys. Rev. Lett.* **124**, 027205 (2020).
- [60] Y. Komijani and P. Coleman, Emergent critical charge fluctuations at the Kondo breakdown of heavy fermions, *Phys. Rev. Lett.* **122**, 217001 (2019).
- [61] P. Sun and G. Kotliar, Understanding the heavy fermion phenomenology from a microscopic model, *Phys. Rev. Lett.* **95**, 016402 (2005).
- [62] D. Tanasković, K. Haule, G. Kotliar, and V. Dobrosavljević, Phase diagram, energy scales, and non-local correlations in the Anderson lattice model, *Phys. Rev. B* **84**, 115105 (2011).
- [63] L. De Leo, M. Civelli, and G. Kotliar, Cellular dynamical mean-field theory of the periodic Anderson model, *Phys. Rev. B* **77**, 075107 (2008).
- [64] L. De Leo, M. Civelli, and G. Kotliar, $T = 0$ heavy-fermion quantum critical point as an orbital-selective Mott transition, *Phys. Rev. Lett.* **101**, 256404 (2008).
- [65] G. Kotliar, S. Y. Savrasov, G. Pálsson, and G. Biroli, Cellular dynamical mean field approach to strongly correlated systems, *Phys. Rev. Lett.* **87**, 186401 (2001).

- [66] K. G. Wilson, The renormalization group: Critical phenomena and the Kondo problem, *Rev. Mod. Phys.* **47**, 773 (1975).
- [67] R. Bulla, T. A. Costi, and T. Pruschke, Numerical renormalization group method for quantum impurity systems, *Rev. Mod. Phys.* **80**, 395 (2008).
- [68] A. Weichselbaum and J. von Delft, Sum-rule conserving spectral functions from the numerical renormalization group, *Phys. Rev. Lett.* **99**, 076402 (2007).
- [69] A. Weichselbaum, Tensor networks and the numerical renormalization group, *Phys. Rev. B* **86**, 245124 (2012).
- [70] S.-S. B. Lee and A. Weichselbaum, Adaptive broadening to improve spectral resolution in the numerical renormalization group, *Phys. Rev. B* **94**, 235127 (2016).
- [71] S.-S. B. Lee, J. von Delft, and A. Weichselbaum, Doublon-holon origin of the subpeaks at the Hubbard band edges, *Phys. Rev. Lett.* **119**, 236402 (2017).
- [72] B. A. Jones, C. M. Varma, and J. W. Wilkins, Low-temperature properties of the two-impurity Kondo Hamiltonian, *Phys. Rev. Lett.* **61**, 125 (1988).
- [73] B. A. Jones and C. M. Varma, Critical point in the solution of the two magnetic impurity problem, *Phys. Rev. B* **40**, 324 (1989).
- [74] I. Affleck and A. W. W. Ludwig, Exact critical theory of the two-impurity Kondo model, *Phys. Rev. Lett.* **68**, 1046 (1992).
- [75] I. Affleck, A. W. W. Ludwig, and B. A. Jones, Conformal-field-theory approach to the two-impurity Kondo problem: Comparison with numerical renormalization-group results, *Phys. Rev. B* **52**, 9528 (1995).
- [76] B. A. Jones, Kondo effect, in *Handbook of Magnetism and Advanced Magnetic Materials*, edited by H. Kronmüller and S. Parkin (Wiley, New York, 2007), Vol. 1, 10.1002/9780470022184.hmm106.
- [77] A. K. Mitchell and E. Sela, Universal low-temperature crossover in two-channel Kondo models, *Phys. Rev. B* **85**, 235127 (2012).
- [78] A. K. Mitchell, E. Sela, and D. E. Logan, Two-channel Kondo physics in two-impurity Kondo models, *Phys. Rev. Lett.* **108**, 086405 (2012).
- [79] O. Sakai, Y. Shimizu, and T. Kasuya, Excitation spectra of two impurity Anderson model, *Solid State Commun.* **75**, 81 (1990).
- [80] O. Sakai and Y. Shimizu, Excitation spectra of the two impurity Anderson model. I. Critical transition in the two magnetic impurity problem and the roles of the parity splitting, *J. Phys. Soc. Jpn.* **61**, 2333 (1992).
- [81] J. B. Silva, W. L. C. Lima, W. C. Oliveira, J. L. N. Mello, L. N. Oliveira, and J. W. Wilkins, Particle-hole asymmetry in the two-impurity Kondo model, *Phys. Rev. Lett.* **76**, 275 (1996).
- [82] M. Fabrizio, A. F. Ho, L. D. Leo, and G. E. Santoro, Non-trivial fixed point in a twofold orbitally degenerate Anderson impurity model, *Phys. Rev. Lett.* **91**, 246402 (2003).
- [83] L. D. Leo and M. Fabrizio, Spectral properties of a two-orbital Anderson impurity model across a non-Fermi-liquid fixed point, *Phys. Rev. B* **69**, 245114 (2004).
- [84] R. M. Fye, anomalous fixed point behavior of two Kondo impurities: A reexamination, *Phys. Rev. Lett.* **72**, 916 (1994).
- [85] A. Nejati, K. Ballmann, and J. Kroha, Kondo destruction in RKKY-coupled Kondo lattice and multi-impurity systems, *Phys. Rev. Lett.* **118**, 117204 (2017).
- [86] B. Lechtenberg, F. Eickhoff, and F. B. Anders, Realistic quantum critical point in one-dimensional two-impurity models, *Phys. Rev. B* **96**, 041109(R) (2017).
- [87] F. Eickhoff, B. Lechtenberg, and F. B. Anders, Effective low-energy description of the two-impurity Anderson model: RKKY interaction and quantum criticality, *Phys. Rev. B* **98**, 115103 (2018).
- [88] F. Eickhoff and F. B. Anders, Strongly correlated multi-impurity models: The crossover from a single-impurity problem to lattice models, *Phys. Rev. B* **102**, 205132 (2020).
- [89] See Supplemental Material at <http://link.aps.org/supplemental/10.1103/PhysRevLett.134.106501> for additional information on the phase diagram and SYK dynamics, basic formulas involving the optical conductivity, the numerical computation of the optical conductivity, the role of vertex contributions, the Drude weight, the scaling functions, and scaling of the complex optical conductivity and an estimate of the suitability of our model parameters for the description of CeCoIn₅, which includes Refs. [90–101].
- [90] P. Nozières, A “Fermi-liquid” description of the Kondo problem at low temperatures, *J. Low Temp. Phys.* **17**, 31 (1974).
- [91] R. Resta, Drude weight and superconducting weight, *J. Phys. Condens. Matter* **30**, 414001 (2018).
- [92] D. J. Scalapino, S. R. White, and S. Zhang, Insulator, metal, or superconductor: The criteria, *Phys. Rev. B* **47**, 7995 (1993).
- [93] A. K. Mitchell, M. R. Galpin, S. Wilson-Fletcher, D. E. Logan, and R. Bulla, Generalized Wilson chain for solving multichannel quantum impurity problems, *Phys. Rev. B* **89**, 121105(R) (2014).
- [94] K. M. Stadler, A. K. Mitchell, J. von Delft, and A. Weichselbaum, Interleaved numerical renormalization group as an efficient multiband impurity solver, *Phys. Rev. B* **93**, 235101 (2016).
- [95] F. B. Kugler, Improved estimator for numerical renormalization group calculations of the self-energy, *Phys. Rev. B* **105**, 245132 (2022).
- [96] Because of singular features developing in the self-consistent hybridization function close to the QCP [56], it is numerically not possible to tune exactly to the QCP.
- [97] A. Weichselbaum, Non-Abelian symmetries in tensor networks: A quantum symmetry space approach, *Ann. Phys. (N.Y.)* **327**, 2972 (2012).
- [98] A. Weichselbaum, X-symbols for non-Abelian symmetries in tensor networks, *Phys. Rev. Res.* **2**, 023385 (2020).
- [99] A. Weichselbaum, QSpace—an open source tensor library for Abelian and non-Abelian symmetries, *SciPost Phys. Codebases* **40** (2024).
- [100] We call frequency dependences $(\omega^a - 1)/a$ with $a \simeq 0$ logarithmic if the exponent a cannot be reasonably distinguished from $a \rightarrow 0$ based on our numerical data. Ditto for temperature dependences. Similarly, “plateau” means ω^a with $a \simeq 0$ and “linear” ω^a with $a \simeq 1$.
- [101] S.-S. B. Lee, F. B. Kugler, and J. von Delft, Computing local multipoint correlators using the numerical renormalization group, *Phys. Rev. X* **11**, 041007 (2021).

- [102] F. B. Kugler, S.-S. B. Lee, and J. von Delft, Multipoint correlation functions: Spectral representation and numerical evaluation, *Phys. Rev. X* **11**, 041006 (2021).
- [103] J.-M. Lihm, J. Halbinger, J. Shim, J. von Delft, F. B. Kugler, and S.-S. B. Lee, Symmetric improved estimators for multipoint vertex functions, *Phys. Rev. B* **109**, 125138 (2024).
- [104] In the PAM, $\mathbf{G}_{\mathbf{k}}(\omega)$ is matrix valued in the orbital space, with orbital index $\alpha \in \{f, c\}$. $G_{\mathbf{k}_F}^{-1}(\omega)$ is defined in terms of the eigenvalue which fulfills $\text{Re}G_{\mathbf{k}_F}^{-1}(0) = 0$. To determine the single-particle decay rate γ^* , the ω dependence of the corresponding eigenvalue is fitted to a Lorentzian line shape around $\omega = 0$, $G_{\mathbf{k}_F}(\omega) \simeq Z/(\omega + i\gamma^*)$, as usual.
- [105] P. Coleman, *Introduction to Many-Body Physics* (Cambridge University Press, Cambridge, England, 2015).
- [106] L. Y. Shi, Z. Tagay, J. Liang, K. Duong, Y. Wu, F. Ronning, D. G. Schlom, K. Shen, and N. P. Armitage, Low energy electrodynamics and a hidden Fermi liquid in the heavy-fermion CeCoIn₅, [arXiv:2310.10916](https://arxiv.org/abs/2310.10916).

Supplemental Material for

“Dynamical scaling and Planckian dissipation due to heavy-fermion quantum criticality”

Andreas Gleis,^{1,2,*} Seung-Sup B. Lee,^{3,4,5,1,†} Gabriel Kotliar,^{2,6,‡} and Jan von Delft^{1,§}

¹*Arnold Sommerfeld Center for Theoretical Physics, Center for NanoScience, and Munich Center for Quantum Science and Technology, Ludwig-Maximilians-Universität München, 80333 Munich, Germany*

²*Department of Physics and Astronomy, Rutgers University, Piscataway, NJ 08854, USA*

³*Department of Physics and Astronomy, Seoul National University, Seoul 08826, Korea*

⁴*Center for Theoretical Physics, Seoul National University, Seoul 08826, Korea*

⁵*Institute for Data Innovation in Science, Seoul National University, Seoul 08826, Korea*

⁶*Condensed Matter Physics and Materials Science Department, Brookhaven National Laboratory, Upton, NY 11973, USA*

(Dated: January 28, 2025)

Section S-I discusses the phase diagram in the vicinity of the QCP and SYK-like dynamics for unscreened fluctuations. In Sec. S-II, we provide basic definitions and expressions regarding the Fourier transforms of operators and regarding the optical conductivity. Section S-III provides additional information on the numerical computation of the optical conductivity, the role of vertex contributions, and to what extent the Drude term vanishes. Section S-IV provides more information on the scaling functions \mathcal{X} and \mathcal{S} . In Sec. S-V, we discuss scaling of the imaginary part of the optical conductivity. Finally, Sec. S-VI provides a rough estimate to what extent our model parameter choice is suitable for the description of CeCoIn₅.

S-I. PHASE DIAGRAM AND SYK-LIKE DYNAMICS

A. Phase diagram

Figure S1(a) shows our 2CDMFT+NRG phase diagram in the (V, T) plane close to the KB-QCP. At $T = 0$, we find two Fermi liquid (FL) phases, separated by a KB-QCP located at $V_c = 0.4575(25)$, featuring a sudden Fermi surface (FS) reconstruction [56]. At finite excitation energies, we find two crossover scales, $T_{\text{FL}}(V)$ and $T_{\text{NFL}}(V)$ [56]. FL behavior emerges below T_{FL} , which decreases towards and vanishes at V_c . The high-energy region above T_{NFL} is characterized by thermally fluctuating f -electron local moments decoupled from the c electrons. T_{NFL} does not decrease for V near V_c , hence strong scale separation between T_{NFL} and T_{FL} occurs close to the QCP. For excitation energies between T_{FL} and T_{NFL} , we find NFL behavior—the main subject of this work.

B. Dynamical susceptibilities

The different regions can be most conveniently distinguished in terms of the dynamical behavior of response functions. For now, we focus on the staggered

f -electron spin on a two-site cluster, $X^{xz} = S_1^z - S_2^z$, with $S_i^z = \frac{1}{2}[f_{i\uparrow}^\dagger f_{i\uparrow} - f_{i\downarrow}^\dagger f_{i\downarrow}]$. The color scale in Fig. S1(a) shows the exponent α of the imaginary-time autocorrelation function of X^{xz} , $\langle X^{xz}(\tau)X^{xz} \rangle \propto \tau^{-\alpha}$, obtained via log-derivative. For long times, $\tau^{-1} < T_{\text{FL}}$, we find $\alpha = 2$, consistent with FL behavior and the presence of long-lived quasi-particles (QP) [3] and thus quickly decaying, localized spin excitations. For short times, $\tau^{-1} > T_{\text{NFL}}$, staggered-spin excitations decay very slowly with an exponent $\alpha < 0.5$, consistent with local moment behavior. For intermediate times, $T_{\text{FL}} < \tau^{-1} < T_{\text{NFL}}$, we find an SYK-like exponent $\alpha \simeq 1$ in the NFL region, indicative of the absence of coherent QP [3]. At $V = 0.46$, our data closest to V_c , this behavior extends over almost 4 orders of magnitude: in fact, our data suggests that it extends down to $\tau^{-1} \rightarrow 0$ at V_c , where $T_{\text{FL}} = 0$. We note that we do *not* find $\propto \tau^{-1/2}$ behavior of the single-electron Green’s function $G(\tau)$, in contrast to the SYK model [3]. Thus, $\langle X^{xz}(\tau)X^{xz} \rangle$ is not $\propto G(\tau)^2$, i.e., the τ^{-1} behavior is governed by vertex contributions.

To understand the origin of the τ^{-1} dependence, we consider the spectral representation of bosonic correlators,

$$\langle \mathcal{A}(\tau)\mathcal{B}^\dagger \rangle = \int_{-\infty}^{\infty} d\omega \frac{e^{-\tau\omega}}{1 - e^{-\beta\omega}} \chi''[\mathcal{A}, \mathcal{B}](\omega). \quad (\text{S1})$$

Here, the spectrum $\chi''(\omega)$ is obtained from the dynamical susceptibility $\chi(\omega) = \chi'(\omega) - i\pi\chi''(\omega)$, see Eq. (2) in the main text.

The spectra for X^{xz} and for the total spin $S^z = S_1^z + S_2^z$ are shown in Fig. S1(b) at $V = 0.46$ and $T = 0$. The spectra $\chi''[X^{xz}]$ and $\chi''[S^z]$ both show $\propto \omega$ behavior below T_{FL} , indicating that these fluctuations are screened in the FL, as expected. For long times, $\tau^{-1} < T_{\text{FL}}$, the corresponding imaginary time correlation function (S1) therefore decays as τ^{-2} , as shown for X^{xz} in Fig. S1(a).

In the NFL region ($T_{\text{FL}} < \omega < T_{\text{NFL}}$) the spectra differ qualitatively: while $\chi''[S^z] \propto \omega$ still holds, $\chi''[X^{xz}]$ has an ω -independent plateau; hence S^z fluctuations are screened, X^{xz} fluctuations are over-screened (reminiscent of the two-channel or two-impurity Kondo models [72, 73, 90]). For intermediate times $\langle S^z(\tau)S^z \rangle$ thus decays as τ^{-2} (not shown) whereas $\langle X^{xz}(\tau)X^{xz} \rangle$ decays as

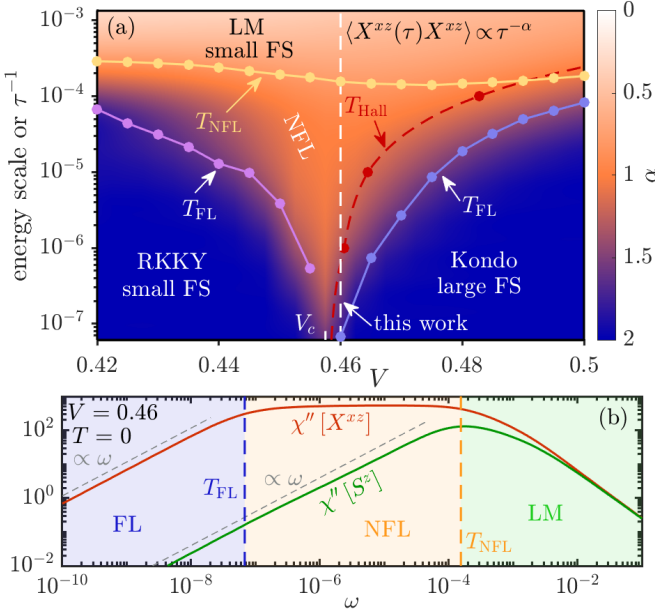


FIG. S1. (a) Phase diagram of the PAM obtained by 2CDMFT+NRG. The dots (connected by lines as guides to the eye) denote relevant energy scales T_{FL} and T_{NFL} below which we observe FL and NFL behavior, respectively, and T_{Hall} , the crossover scale between a large and small FS (see Ref. [56] for details). The color scale denotes the exponent α of the imaginary-time correlator $\langle X^{xz}(\tau)X^{xz} \rangle \propto \tau^{-\alpha}$. The white dashed line denotes $V = 0.46$, used for all subsequent plots in this work. (b) Spectra of X^{xz} and S^z at $T = 0$.

τ^{-1} [cf. Fig. S1(a)]. We note that besides X^{xz} , many other operators also have plateaus in their spectra, see Fig. 4 in Ref. [56]. Thus, the FL is reached via a two-stage screening process: as ω drops below T_{NFL} , some excitations are screened, others over-screened; below T_{FL} , the latter are screened, too.

S-II. OPTICAL CONDUCTIVITY

In this section, we state some textbook [111] formulas that are important in the context of the optical conductivity for the PAM.

A. Fourier transforms of operators

We define the Fourier transform of fermionic creation and annihilation operators in a unitary fashion,

$$c_{\mathbf{k}\sigma} = \frac{1}{\sqrt{N}} \sum_i e^{-i\mathbf{k}\cdot\mathbf{r}_i} c_{i\sigma}, \quad (\text{S2})$$

ensuring $\{c_{\mathbf{k}\sigma}^\dagger, c_{\mathbf{k}'\sigma'}\} = \delta_{\sigma\sigma'}\delta_{\mathbf{k}\mathbf{k}'}$. For bosonic observables \mathcal{O}_i like the current density, on the other hand, we define it as an orthogonal but non-unitary transformation,

$$\mathcal{O}_{\mathbf{q}} = \frac{1}{N} \sum_i e^{-i\mathbf{q}\cdot\mathbf{r}_i} \mathcal{O}_i. \quad (\text{S3})$$

This ensures that the expectation values $\langle \mathcal{O}_{\mathbf{q}} \rangle$ and $\langle \mathcal{O}_i \rangle$ scale the same way with N in the thermodynamic limit. (if we had used a unitary Fourier transforms for bosonic observables, $\langle \mathcal{O}_{\mathbf{q}} \rangle \sim \sqrt{N}$ would not be well-defined in the thermodynamic limit). The same goes for source fields like the vector potential.

B. Current and conductivity

In presence of a vector potential \mathbf{A} , the Hamiltonian (1) is modified by replacing the hopping between site i and $i + \mathbf{a}$ by $t \rightarrow t \exp(-ieA_i^a)$, where \mathbf{a} is some unit lattice vector. The current density is

$$j_i^a = -\frac{\partial H}{\partial A_i^a} = -ite \sum_{\sigma} \left(e^{-ieA_i^a} c_{i\sigma}^\dagger c_{i+\mathbf{a}\sigma} - \text{h.c.} \right). \quad (\text{S4})$$

If no lattice symmetry is broken, the current response to a \mathbf{q} - and ω -dependent electric field $\mathbf{E}_{\mathbf{q}}(\omega) = i\omega^+ \mathbf{A}_{\mathbf{q}}(\omega)$ (where $\omega^+ = \omega + i0^+$) takes the form $\langle j_{\mathbf{q}}^a \rangle(\omega) = \sigma_{\mathbf{q}}(\omega) E_{\mathbf{q}}^a(\omega)$, where the dynamical conductivity is given by

$$\sigma_{\mathbf{q}}(\omega) = \frac{1}{i\omega^+} [\langle \hat{K} \rangle - \chi[j_{\mathbf{q}}^a](\omega)], \quad (\text{S5})$$

$$\hat{K} = -\frac{te^2}{N} \sum_{i\sigma} (c_{i\sigma}^\dagger c_{i+\mathbf{a}\sigma} + \text{h.c.}),$$

and $j_{\mathbf{q}}^a = \frac{1}{N} \sum_i e^{-i\mathbf{q}\cdot\mathbf{r}_i} j_i^a$. In a d -dimensional hypercubic lattice, $\langle \hat{K} \rangle$ is proportional to the kinetic energy density $\epsilon_{\text{kin}} = \frac{d}{e^2} \langle \hat{K} \rangle$.

The optical conductivity $\sigma(\omega) = \sigma_{\mathbf{q}=\mathbf{0}}(\omega)$ is the response to a uniform electric field. It can be decomposed as [91, 92] $\sigma(\omega) = \sigma^D(\omega) + \sigma^{\text{reg}}(\omega)$, with

$$\sigma^D(\omega) = D \left[\delta(\omega) + \mathcal{P} \frac{i}{\pi\omega} \right], \quad (\text{S6})$$

$$D = \pi [\chi'[j_{\mathbf{0}}^a](0) - \langle \hat{K} \rangle], \quad (\text{S7})$$

$$\sigma^{\text{reg}}(\omega) = \mathcal{P} \frac{1}{i\omega} [\chi'[j_{\mathbf{0}}^a](0) - \chi[j_{\mathbf{0}}^a](\omega)], \quad (\text{S8})$$

where \mathcal{P} denotes the principal part. The regular term $\sigma^{\text{reg}}(\omega)$ describes currents that decay at long times; the Drude term $\sigma^D(\omega)$ with Drude weight D describes persistent currents. For a non-superconducting, thermodynamically large lattice model at non-zero temperature, one expects $D = 0$.

The optical conductivity fulfills the f -sum rule,

$$\int_{-\infty}^{\infty} \frac{d\omega}{\pi} \sigma'(\omega) = -\langle \hat{K} \rangle, \quad (\text{S9})$$

which follows when evaluating $\chi'[j_{\mathbf{0}}^a](0)$ using the Kramers-Kronig relation for general susceptibilities,

$$\chi'[\mathcal{O}](\omega') = -\mathcal{P} \int_{-\infty}^{\infty} d\omega \chi''[\mathcal{O}](\omega) / (\omega - \omega'). \quad (\text{S10})$$

C. Bubble contribution

The bubble contribution to the current susceptibility is defined as the susceptibility of a free system but with the Green's functions replaced by the Green's function of the interacting system. We shortly outline the corresponding formulas for the bubble contribution to the local current susceptibility, $\chi_B[j_i^a]$ and to the uniform $\mathbf{q} = 0$ susceptibility, $\chi_B[j_0^a]$. Since the current operator in Eq. (S4) consists only of c -electron operators, the formulas for the bubble contribution only involve c -electron Green's functions. For brevity, we suppress the c labels on all Green's functions, spectral functions and self-energies in this section and in Sec. S-III A. The current operators can be written in terms of the bare current vertex \mathcal{J}^a ,

$$j_i^a = \sum_{\ell\ell'\sigma} \mathcal{J}_{i\ell\ell'}^a c_{\ell\sigma}^\dagger c_{\ell'\sigma}, \quad (\text{S11a})$$

$$\mathcal{J}_{i\ell\ell'}^a = -ite (\delta_{i\ell}\delta_{i+\mathbf{a}\ell'} - \delta_{i+\mathbf{a}\ell}\delta_{i\ell'}), \quad (\text{S11b})$$

$$j_{\mathbf{q}}^a = \frac{1}{N} \sum_i e^{-i\mathbf{q}\cdot\mathbf{r}_i} j_i^a = \sum_{\mathbf{k}\mathbf{k}'\sigma} \mathcal{J}_{\mathbf{q}\mathbf{k}\mathbf{k}'}^a c_{\mathbf{k}\sigma}^\dagger c_{\mathbf{k}'\sigma}, \quad (\text{S11c})$$

$$\mathcal{J}_{\mathbf{q}\mathbf{k}\mathbf{k}'}^a = \frac{-2te}{N} \delta_{\mathbf{q},\mathbf{k}-\mathbf{k}'} e^{i\frac{\mathbf{q}\cdot\mathbf{a}}{2}} \sin\left[\left(\mathbf{k} - \frac{\mathbf{q}}{2}\right) \cdot \mathbf{a}\right]. \quad (\text{S11d})$$

We define the polarization bubble (with $\text{Im } z > 0$),

$$\mathcal{P}_{g,g'}(z) = T \sum_m G_g(i\omega_m) G_{g'}(i\omega_m + z) \quad (\text{S12})$$

$$= \int_{-\infty}^{\infty} d\omega f(\omega) [A_g(\omega) G_{g'}(\omega + z) + A_{g'}(\omega) G_g(\omega - z)], \quad (\text{S13})$$

where $G(z)$ is the Green's function, $A(\omega)$ the corresponding spectral function, $f(\omega)$ the Fermi-Dirac distribution function and g and g' are quantum numbers like momentum, spin or spatial distance, $\mathbf{r}_{ij} = \mathbf{r}_i - \mathbf{r}_j$ and we assume G depends on $|\mathbf{r}_i - \mathbf{r}_j|$ only.

The bubble contribution to the $\mathbf{q} = 0$ current susceptibility is

$$\begin{aligned} \chi_B[j_0^a](z) &= \frac{8t^2 e^2}{N} \sum_{\mathbf{k}} \sin^2(\mathbf{k} \cdot \mathbf{a}) \mathcal{P}_{\mathbf{k},\mathbf{k}}(z) \\ &= \frac{8t^2 e^2}{N} \sum_{\mathbf{k}} \sin^2(\mathbf{k} \cdot \mathbf{a}) \int_{-\infty}^{\infty} d\omega f(\omega) \times \\ &\quad [A_{\mathbf{k}}(\omega) G_{\mathbf{k}}(\omega + z) + A_{\mathbf{k}}(\omega) G_{\mathbf{k}}(\omega - z)]. \end{aligned} \quad (\text{S14})$$

The corresponding spectral function is ($\nu^\pm = \nu \pm i0^+$)

$$\begin{aligned} \chi_B''[j_0^a](\nu) &= \frac{i}{2\pi} [\chi_B[j_0^a](\nu^+) - \chi_B[j_0^a](\nu^-)] \\ &= \frac{8t^2 e^2}{N} \sum_{\mathbf{k}} \sin^2(\mathbf{k} \cdot \mathbf{a}) I_{\mathbf{k}}(\nu) \end{aligned} \quad (\text{S15a})$$

$$I_{\mathbf{k}}(\nu) = \int_{-\infty}^{\infty} d\omega [f(\omega) - f(\omega + \nu)] A_{\mathbf{k}}(\omega) A_{\mathbf{k}}(\omega + \nu). \quad (\text{S15b})$$

The bubble contribution to the local current-current susceptibility (involving one link in the lattice, i.e., two sites) is then

$$\begin{aligned} \chi_B[j_i^a](z) &= 2 \sum_{mm'} \sum_{nn'} \mathcal{J}_{imm'}^a \mathcal{J}_{inn'}^a \mathcal{P}_{\mathbf{r}_{m'n'}, \mathbf{r}_{m'n'}}(z) \\ &= -4t^2 e^2 \int_{-\infty}^{\infty} d\omega f(\omega) \times \\ &\quad [[A_{\mathbf{r}_{i,i+\mathbf{a}}}(\omega) G_{\mathbf{r}_{i+\mathbf{a},i}}(\omega + z) - A_{\mathbf{r}_{i,i}}(\omega) G_{\mathbf{r}_{i,i}}(\omega + z)] \\ &\quad + [A_{\mathbf{r}_{i+\mathbf{a},i}}(\omega) G_{\mathbf{r}_{i,i+\mathbf{a}}}(\omega - z) - A_{\mathbf{r}_{i,i}}(\omega) G_{\mathbf{r}_{i,i}}(\omega - z)]]. \end{aligned} \quad (\text{S16})$$

The local current-current spectral function is

$$\chi_B''[j_i^a](\nu) = \frac{i}{2\pi} [\chi_B[j_i^a](\nu^+) - \chi_B[j_i^a](\nu^-)] \quad (\text{S17})$$

$$= 4t^2 e^2 \int_{-\infty}^{\infty} d\omega [f(\omega) - f(\omega + \nu)] \times \quad (\text{S18})$$

$$[A_{\mathbf{r}_{i,i}}(\omega) A_{\mathbf{r}_{i,i}}(\omega + \nu) - A_{\mathbf{r}_{i,i+\mathbf{a}}}(\omega) A_{\mathbf{r}_{i+\mathbf{a},i}}(\omega + \nu)].$$

S-III. OPTICAL CONDUCTIVITY: NUMERICAL COMPUTATION

In this section, we describe how we compute the bubble contribution $\chi_B''[j_0^a](\nu)$ [Eq. (S15a)] in a numerically efficient way, how we treat the electronic self-energy close to zero frequency and temperature, and how we deal with vertex contributions and fulfillment of the f sum rule. We further discuss the potential role of vertex contributions for short-ranged nonlocal current fluctuations.

A. Bubble contribution

Computing the bubble contribution to the optical conductivity requires numerical evaluation of Eq. (S15a). This is challenging, especially close to $\nu = 0$ or $T = 0$, due to the close-to-singular behavior of $A_{\mathbf{k}}(\omega) A_{\mathbf{k}}(\omega + \nu)$ in the integrand.

To deal with this, we exploit our knowledge of $G_{\mathbf{k}}^{-1}(\omega^+) = \omega^+ + \mu - \epsilon_{\mathbf{k}} - \Sigma_{\mathbf{k}}(\omega^+)$. It is a smooth function of ω and known on a predetermined frequency grid $\omega \in \{\omega_i\}$. Since $G_{\mathbf{k}}^{-1}(\omega^+)$ is a smooth function, we represent it by linear interpolation, $G_{\mathbf{k}}^{-1}(\omega^+) = a_i + b_i \omega$, for $I_i = [\omega_i, \omega_{i+1}]$. Due to the logarithmic resolution of NRG, we use a logarithmic frequency grid with $10^{-12} \leq |\omega_i| \leq 10^4$ and 200 grid points per decade.

By writing

$$\begin{aligned} A_{\mathbf{k}}(\omega) A_{\mathbf{k}}(\omega + \nu) &= \\ &= \frac{1}{\pi} \text{Im} \left[G_{\mathbf{k}}(\omega^+) \frac{G_{\mathbf{k}}(\omega + \nu^+) - G_{\mathbf{k}}(\omega + \nu^-)}{2\pi i} \right], \end{aligned} \quad (\text{S19})$$

the frequency integral in Eq. (S15b) can be computed by evaluating the integrals,

$$I_{\mathbf{k}}^\pm(\nu) = \int_{-\infty}^{\infty} d\omega [f(\omega) - f(\omega + \nu)] G_{\mathbf{k}}(\omega^+) G_{\mathbf{k}}(\omega + \nu^\pm)$$

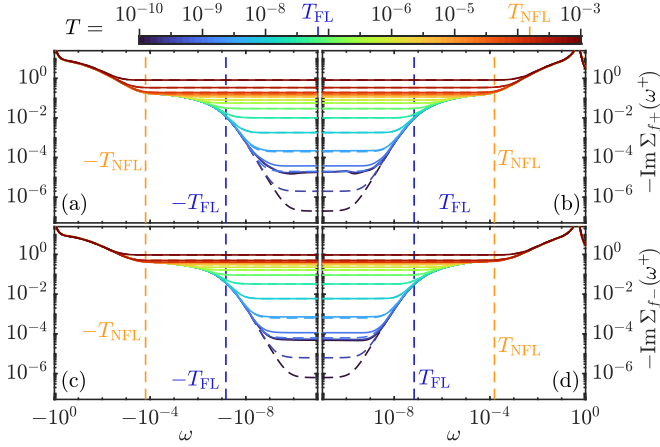


FIG. S2. Self-energy of the f electrons for the self-consistent 2IAM at different temperatures. (a,b) Bonding orbital (+) and (c,d) anti-bonding orbital (-). Solid lines denote the numerical data, dashed lines (not visible whenever they coincide with solid lines) denote the extrapolated self-energy. Visible differences occur only for $|\omega|, T < 10^{-1}T_{\text{FL}}$, i.e., well below the FL scale T_{FL} .

$$= \sum_i \int_{I_i} d\omega \frac{\alpha_i + \beta_i \omega}{(a_i + b_i \omega)(c_{i,\pm} + d_{i,\pm} \omega)}, \quad (\text{S20})$$

where $\alpha_i + \beta_i \omega$ is a linear interpolation of $f(\omega) - f(\omega + \nu)$ on the interval I_i and $a_i + b_i \omega$ and $c_{i,\pm} + d_{i,\pm} \omega$ are the linear interpolations of $G_{\mathbf{k}}^{-1}(\omega^+)$ and $G_{\mathbf{k}}^{-1}(\omega + \nu^\pm)$, respectively. The integral over every interval I_i in Eq. (S20) is very simple to evaluate exactly, summing up the contributions from all intervals gives $I_{\mathbf{k}}^\pm(\nu)$.

The \mathbf{k} sum/integral in Eq. (S15a) is finally computed using a standard integrator. (We use MATLAB's `integral` function.) We use the periodized self-energy when computing Eq. (S15a), cf. App. A.3 of Ref. [56]. In our case, this allows us to reduce the three-dimensional \mathbf{k} integral in Eq. (S15a) to a one-dimensional one, cf. Eq. (A10) of Ref. [56].

B. Self-energy at $\omega, T \simeq 0$

The Drude peak which emerges in the optical conductivity at $T < T_{\text{FL}}$ for small frequencies arises due to $-\text{Im}\Sigma(\omega^+) = a\omega^2 + bT^2$ behavior for $|\omega|, T < T_{\text{FL}}$. Capturing this ω, T -dependence for very small $T_{\text{FL}} (\ll T_{\text{NFL}})$, as is the current case close to the QCP, is highly challenging. To achieve this, we keep a large number of states—up to 40,000 $U(1) \times \text{SU}(2)$ symmetry multiplets—in iterative diagonalization and use an interleaved Wilson chain [93, 94] to keep the computational cost manageable. We compute the f -electron self-energy by using the symmetric improved estimator of Ref. [95] which significantly reduces numerical artifacts and leads to state-of-the-art accuracy. This accuracy allows us to obtain $-\text{Im}\Sigma_{f\pm}(\omega^+) = a\omega^2 + bT^2$ behavior for $|\omega|, T \in (T_{\text{FL}}/10, T_{\text{FL}})$ (but not for $|\omega|, T \in (0, T_{\text{FL}}/10)$, because there $-\text{Im}\Sigma_{f\pm}(\omega^+)$ becomes

smaller than 10^{-4} , and numerical inaccuracies become significant). Therefore, we fit the coefficients a and b with the data for $(T_{\text{FL}}/10, T_{\text{FL}})$ then extrapolate $-\text{Im}\Sigma_{f\pm}(\omega^+)$ to $(0, T_{\text{FL}}/10)$ based on the fitting. Figure S2 shows the low T and ω behavior of $-\text{Im}\Sigma_{f\pm}(\omega^+)$ before (solid) and after (dashed) extrapolation. The c -electron self-energy $\Sigma_{c\pm}(\omega^+) = V^2/(\omega^+ - \epsilon_f - \Sigma_{f\pm}(\omega^+))$ (which is not one-particle irreducible) follows from $\Sigma_{f\pm}(\omega^+)$.

Note that in an FL, $a\pi^2/b = 1$ should hold. On the other hand, our fits yield $a\pi^2/b = \mathcal{O}(2-3)$ due to the broadening used in NRG, which overestimates a . We have checked that $a \rightarrow b/\pi^2$ when we lower the broadening width. This however comes at the expense of severe discretization artifacts. Since the exact value of a is irrelevant to the present work, we preferred to adopt the procedure described above.

C. Local vertex contributions

We stated several times in the main text that vertex contributions are crucial for the current-current correlation functions to capture the strange metallicity and Planckian dissipation. As described in the main text, we have included vertex contributions only for the local contribution, $\chi[j_i^a]$, to the uniform current susceptibility, $\chi[j_0^a] = \chi[j_i^a] + \chi_{\text{nl}}[j_0^a]$, where $j_i^a = -ite \sum_{\sigma} (c_{i\sigma}^\dagger c_{i+\mathbf{a}\sigma} - \text{h.c.})$ is the current between lattice sites i and $i + \mathbf{a}$, the neighbor of i in a -direction. We explain in Sec. S-III E why the full nonlocal vertex contributions are currently out of reach. By choosing sites i and $i + \mathbf{a}$ as the two sites of our self-consistent two-impurity model, we can compute $\chi[j_i^a]$ directly as a two-point correlation function using NRG. Here, we provide supplemental data that shows to what extent the full local susceptibility $\chi[j_i^a]$ is influenced by its vertex contribution $\chi_{\text{vtx}}[j_i^a] = \chi[j_i^a] - \chi_{\text{B}}[j_i^a]$. To this end, we compare $\chi[j_i^a]$ to its bubble contribution $\chi_{\text{B}}[j_i^a]$, computed via Eq. (S18). The integrand of the latter is *not* close-to-singular [in contrast to that of Eq. (S15b)] and can therefore be efficiently evaluated via a standard integrator.

The bare output of NRG are discrete spectra for $\chi''[j_i^a]$, which are subsequently broadened through log-Gaussian broadening kernels, see Ref. [70] for more details. The spectral functions used in Eq. (S18) to compute $\chi_{\text{B}}''[j_i^a]$ on the other hand are obtained by computing the *self-energy* via the symmetric improved estimators of Ref. [95]; $\chi_{\text{B}}''[j_i^a]$ therefore contains finer high-frequency details than achievable with NRG for $\chi''[j_i^a]$. To compare the full $\chi''[j_i^a]$ and its bubble contribution $\chi_{\text{B}}''[j_i^a]$ [computed from Eq. (S18)], we, therefore, smear out the continuous curve of $\chi_{\text{B}}''[j_i^a]$ by further applying the log-Gaussian kernel used to broaden the discrete data for $\chi''[j_i^a]$, to match their resolution levels. We emphasize here that this broadening of $\chi_{\text{B}}''[j_i^a]$ only affects high-frequency details at $|\omega| > T_{\text{NFL}}$, the basic features remain the same.

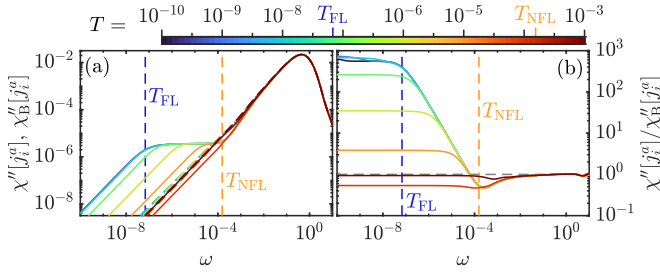


FIG. S3. (a) Spectrum of the local current susceptibility $\chi''[j_i^a](\omega, T)$. Solid lines are full susceptibilities $\chi''[j_i^a]$, dashed lines are the bubble contributions $\chi_B''[j_i^a]$. $\chi_B''[j]$ is almost temperature independent, which is why the $\chi_B''[j_i^a]$ curves for $T < 10^{-3}$ are covered by the $T = 10^{-3}$ curve. $\chi_B''[j_i^a]$ and $\chi''[j_i^a]$ are almost identical at $T = 10^{-3}$. (b) The ratio between full susceptibility and bubble contribution.

Figure S3(a) shows the spectrum of the full local current susceptibility $\chi''[j_i^a]$ and of the corresponding bubble contribution $\chi_B''[j_i^a]$, while Fig. S3(b) shows their ratio. The bubble contribution captures only the high-frequency behavior at $|\omega|, T > T_{\text{NFL}}$ well: the spectra in Fig. S3(a) almost coincide and the ratios in Fig. S3(b) are close to 1.

On the other hand, the plateau emerging below $|\omega|, T < T_{\text{NFL}}$ is not captured at all by the bubble contribution, i.e., both the ω/T scaling and the Planckian dissipation discussed in the main text and in Sec. S-IV result from vertex contributions. The ratio shown in Fig. S3(b) increases dramatically in the NFL region ($T_{\text{FL}} < |\omega|, T < T_{\text{NFL}}$) by several orders of magnitude and saturates close to 10^3 in the FL region ($|\omega|, T < T_{\text{FL}}$).

D. Estimate of nonlocal vertex contributions

To estimate what to expect for nonlocal current fluctuations in terms of scaling and vertex contributions, we define “current” operators that lie across the cluster boundaries,

$$j_i = (-1)^i \frac{ite}{\sqrt{5}} \left(c_{i\sigma}^\dagger a_{i\sigma} - \text{h.c.} \right), \quad (\text{S21})$$

where $a_{i\sigma}$ annihilates a spin- σ electron in the first bath orbital (within the Wilson chain) that directly couples to the c orbital of the cluster site $i = 1, 2$. According to the effective medium construction of DMFT (which defines bath sites by replacing the interaction on the original lattice sites by the self-energy, cf. Sec. III D of Ref. [40]), the Green’s function of $a_{i\sigma}$ is the same as that of a symmetric superposition of the five nearest neighbors (on the lattice) of site i which are not located on the same cluster. Due to that, we can interpret these orbitals as a proxy for the aforementioned symmetric superposition. The current operators in Eq. (S21) can therefore be interpreted as a proxy for the average (hence normalization by $\sqrt{5}$) current between these five nearest-neighbor sites and the corresponding cluster site. Since

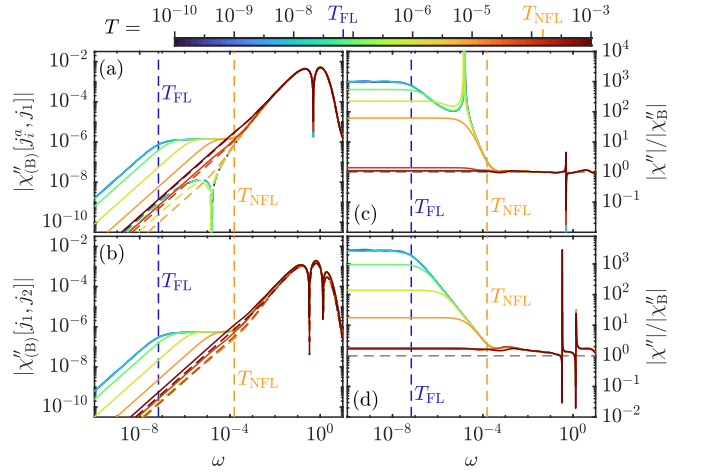


FIG. S4. (a,b) Absolute values of the spectra of different nonlocal current susceptibilities, $\chi''[j_i^a, j_1](\omega, T)$ and $\chi''[j_1, j_2](\omega, T)$. Solid lines are full susceptibilities, dashed lines are the bubble contributions. Cusps indicate sign changes in the spectra. (c,d) Ratios between the spectra of the full susceptibility and the bubble contribution. The cusps at $|\omega| > 10^{-1}$ arise due to a slight misalignment between the sign changes in χ'' and χ_B'' .

there is no specific direction in the lattice associated with these currents, we did not specify a superscript a in Eq. (S21). We emphasize that this correspondence is *not* exact since the first bath sites are non-interacting orbitals that belong to the dynamical mean field. Correlators involving j_1 or j_2 do not enter the results shown in the main text.

We compute $\chi[j_i^a, j_1]$ and $\chi[j_1, j_2]$ to estimate the behavior of nearest-neighbor and next-nearest-neighbor current susceptibilities, respectively. Their spectra, including the corresponding bubble contribution, are shown in Fig. S4(a,b). The spectra of the full susceptibilities again show a similar plateau as observed for the local current susceptibility. Figure S4(c,d) shows the ratio between full susceptibility and bubble contribution. Similarly to the local current susceptibility, the ratio is somewhat close to 1 for $|\omega|, T > T_{\text{NFL}}$ and becomes large for $|\omega|, T < T_{\text{NFL}}$, suggesting that vertex contributions are important also on the nonlocal level in this region.

In Fig. S5, we further illustrate that $\chi''[j_i^a, j_1]$ and $\chi''[j_1, j_2]$ show ω/T scaling very similar to $\chi''[j_i^a]$. Since the behavior of the nonlocal susceptibilities is qualitatively similar to that of the local susceptibility, we expect that the full nonlocal current susceptibility $\chi''_{\text{nl}}[j]$, in contrast to its bubble contribution $\chi_B''_{\text{nl}}[j]$, will show similar ω/T scaling as $\chi''[j_i^a]$. As discussed in the main text, we expect that the full inclusion of vertex contributions in $\chi''_{\text{nl}}[j]$ will ameliorate or fully avoid the artifacts seen in Fig. 2(c) for the resistivity $\rho(T)$: (i) in the NFL region, the nearly- T -linear behavior will become fully- T -linear; and (ii) in the FL-to-NFL crossover region, the shoulder will become less prominent or disappear.

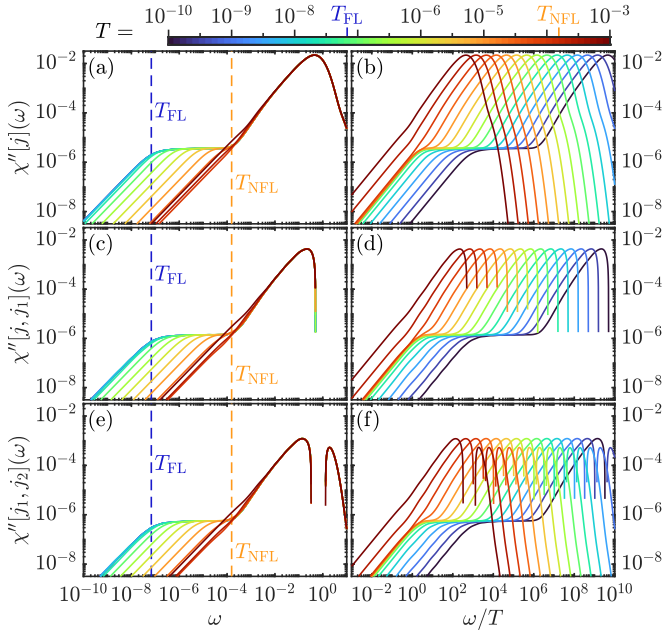


FIG. S5. Current spectra versus frequency (left column) and versus ω/T (right column). (a,b) Local current spectrum. (c,d) Proxy to the nearest-neighbor current spectrum. (e,f) Proxy to the next-nearest-neighbor current spectrum.

E. Full vertex contributions: why they are currently out of reach

In Secs. S-III C–S-III D above [see also Eq. (5) and its discussion in the main text], we demonstrated the relevance of the vertex contributions by computing the *local* vertex contributions and arguing in the spirit of DMFT that the corresponding lattice quantities have weak momentum dependence by computing various correlators. While more rigorous arguments could be made by quantifying *nonlocal* vertex contributions, it goes beyond the reach of our current abilities, regrettably, for the following reasons.

First, one needs to compute the full four-point vertex function at the cluster impurity of the self-consistent 2IAM, which is computationally heavy. Very recently, some of us developed the NRG method for such computation and applied it to one-band impurity models [107, 109]. In these works, the logarithmic discretization parameter Λ has to be chosen comparably large, to allow using a small number of kept states, $N_{\text{keep}} = 300$, and to limit the length of the Wilson chain, $N_{\text{chain}} \simeq 20$. This is desirable since the cost of vertex computations scales as $\mathcal{O}(N_{\text{keep}}^3 N_{\text{chain}}^3)$. Even with this choice, the calculations in Refs. [107, 109] were quite heavy. For the 2IAM used in this study, we have a larger local Hilbert space dimension, requiring $N_{\text{keep}} \gtrsim 10,000$, and we have significantly longer Wilson chains. All of that means that NRG computations of four-point correlation functions for this 2IAM are currently not feasible with reasonable resources.

Second, even if the four-point vertex were obtained from

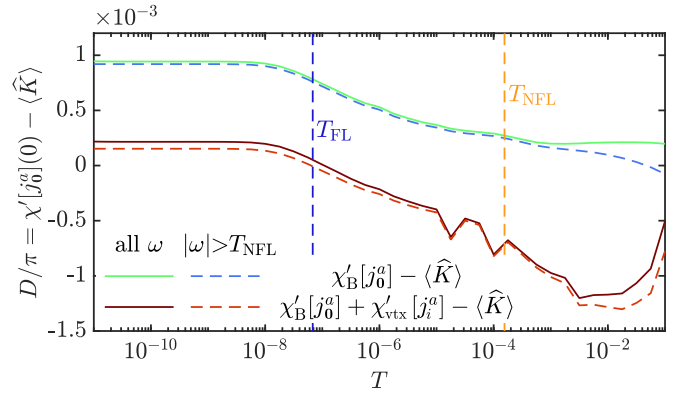


FIG. S6. The Drude weight $D/\pi = \chi'[j_0^a](0) - \langle \hat{K} \rangle$ vs temperature. For the upper (or lower) row of the legend, $\chi'[j_0^a](0)$ was approximated as $\chi'_B[j_0^a](0)$ (or $\chi'_B[j_0^a](0) + \chi'_{\text{vtx}}[j_i^a](0)$), i.e., using only the bubble contribution (or including also the local vertex contribution). When computing these $\chi'[j](0)$ terms via the Kramers–Kronig transformation (S10), we either integrated over all $\omega \in \mathbb{R}$ (solid lines) or only high frequencies $|\omega| > T_{\text{NFL}}$ (dashed lines). Since solid and dashed lines almost match, $\chi'[j](0)$ is governed by high-frequency contributions, where NRG has poorer frequency resolution. From that perspective, the values for the Drude weight found here, $D/\pi \lesssim 10^{-3}$, are remarkably close to the expected value of zero.

the impurity model, it is a matter of current research how to periodize it to obtain the corresponding lattice version.

Third, even if the periodized four-point vertex were available, the computation of *lattice* susceptibilities from the 2CDMFT Green’s functions and local vertex would still require solving non-trivial diagrammatic (e.g., Bethe–Salpeter) equations on the real-frequency axis at extremely low temperatures. This is highly non-trivial and computationally expensive, and will require further development of numerical methodology (e.g., to obtain a compressed representation of the diagrammatic objects) to be feasible in the future.

F. Drude weight

In this section, we discuss the Drude weight of Eq. (S7), $D/\pi = \chi'[j_0^a](0) - \langle \hat{K} \rangle$. According to Eq. (S6), if $D \neq 0$ that would imply (i) a $\delta(\omega)$ contribution to $\sigma'(\omega)$ and therefore zero resistivity (i.e., persistent currents), and (ii) a $1/\omega$ contribution in $\sigma''(\omega)$. Since our study of $\sigma(\omega)$ considers only non-superconducting solutions at $T > 0$, we expect that our system does not support persistent currents and $D = 0$. Accordingly, we have set $D = 0$ for all results shown in this manuscript.

As a consistency check, we have also computed the Drude weight directly. This is a difficult task, since the numerical challenges involved in computing $\chi'[j_0^a](0)$, a *uniform, zero-frequency* susceptibility, and $\langle \hat{K} \rangle$, a *local, equal-time* expectation value, are quite different. Moreover, our computation of $\chi'[j_0^a]$ involves a rather crude

approximation [Eq. (5) of the main text]. Nevertheless, we find $|D|/\pi$ to be remarkably small, $\lesssim 10^{-3}$, with an estimated numerical uncertainty that is likewise of the order of 10^{-3} . This justifies our choice to set $D = 0$. Below, we describe how we obtained these values.

Figure S6 shows the Drude weight D/π , with the static current response $\chi'[j_0^a](0)$ computed via Eq. (5) in the main text. Both the bubble contribution $\chi'_B[j_0^a](0)$ and our locally vertex-corrected result $\chi'_B[j_0^a](0) + \chi'_{\text{vtx}}[j_i^a](0)$ show a deviation from $\langle \hat{K} \rangle$ of the order of 10^{-3} . The inclusion of $\chi'_{\text{vtx}}[j_i^a](0)$ slightly reduces this deviation at low T but slightly increases it at high T . The solid and dashed lines in Fig. S6 compare results obtained by computing the $\chi'[j_0^a](0)$ contributions via the Kramers–Kronig transform (S10) in two ways, either including the spectral weight from all frequencies, $\omega \in \mathbb{R}$ (solid), or only from large frequencies, $|\omega| > T_{\text{NFL}}$ (dashed). Since the solid and dashed lines almost match, the contribution to D from low frequencies $|\omega| < T_{\text{NFL}}$ (including the contribution from the plateau in $\chi''_{\text{vtx}}[j_i^a](\omega)$) is negligible. Therefore, the non-fulfillment of $D = 0$ is mainly due to inaccuracies at high frequencies.

High-frequency inaccuracies are to be expected in NRG spectra, due to the use of logarithmic discretization and an asymmetric log-Gaussian broadening kernel (cf. Eqs. (17) and (21) from Ref. [70]), which can lead to slight shifts in spectral weight. The broadened spectral function is evaluated on a logarithmic frequency grid and approximated by linear interpolation between grid points. In practice, this means that if a discrete spectrum of the form $\chi''(\omega) = \sum_j \chi''_j \delta(\omega - E_j)$ is broadened, the integral of the broadened spectrum can differ slightly from the actual weight, $\sum_j \chi''_j$, typically by an amount $\sim \mathcal{O}(10^{-3})$. As a result, the Kramers–Kronig transformation used to compute $\chi'(0) = -\mathcal{P} \int \chi''(\omega)/\omega$ usually induces an error $\sim \mathcal{O}(10^{-3})$, compared to the result directly computed from the discrete data, $\chi'(0) = -\sum_j \chi''_j/E_j$. Since our approximation of $\chi''[j_0^a](\omega)$ involves the bubble contributions $\chi''_B[j_0^a](\omega)$ and $\chi''_B[j_i^a](\omega)$ which are only available as broadened spectral functions, direct computation of $\chi'_B[j_0^a](0)$ from discrete data is not possible. All of the aforementioned issues, on top of the approximation (5), can lead to inaccuracies in the spectral weights and their corresponding frequencies. We have checked that shifting spectral positions by $\mathcal{O}(1\%)$, i.e., $\omega \rightarrow (1 \pm 10^{-2})\omega$ and normalizing the spectra accordingly, i.e., $\chi''(\omega) \rightarrow (1 \pm 10^{-2})^{-1}\chi''(\omega)$, is sufficient to change $\chi'[j_0^a](0)$ by $\mathcal{O}(10^{-3})$. For all these reasons, we estimate the numerical uncertainty of our determination of the Drude weight D to be at least of the order of 10^{-3} .

S-IV. SCALING FUNCTION

In the main text, we reported that the staggered-spin susceptibility $\chi[X^{xz}] = \chi' - i\pi\chi''$ showed a striking plateau

for its spectrum χ'' , leading to ω/T scaling behavior in the NFL regime ($T_{\text{FL}} < T < T_{\text{NFL}}$, $|\omega| < T_{\text{NFL}}$). We noted that there, χ can be well fitted by a function $\tilde{\chi} = \tilde{\chi}' - i\pi\tilde{\chi}''$ obtained by making a phenomenological ansatz for its imaginary part at positive frequencies,

$$\tilde{\chi}''(\omega > 0, T) = \chi_0 \int_T^{T_{\text{NFL}}} \frac{d\epsilon}{\pi} \frac{(1 - e^{-\frac{\omega}{T}})(\frac{\epsilon}{T})^\nu bT}{(\omega - a\epsilon)^2 + (bT)^2}, \quad (\text{S22})$$

imposing antisymmetry on the imaginary part,

$$\tilde{\chi}''(-\omega, T) = -\tilde{\chi}''(\omega, T), \quad (\text{S23})$$

and defining its real part via the Kramers-Kronig relation

$$\tilde{\chi}'(\omega) = \mathcal{P} \int_{-\infty}^{\infty} d\omega' \frac{\tilde{\chi}''(\omega')}{\omega - \omega'}. \quad (\text{S24})$$

We also noted that the resulting $\tilde{\chi}$ can be expressed as

$$\tilde{\chi}(\omega, T) \simeq \mathcal{X}'_0\left(\frac{T}{T_{\text{NFL}}}\right) + \mathcal{X}'\left(\frac{\omega}{T}\right) - i\pi\mathcal{X}''\left(\frac{\omega}{T}\right), \quad (\text{S25})$$

where \mathcal{X}_0 and $\mathcal{X} = \mathcal{X}' - i\pi\mathcal{X}''$ are universal scaling functions. In this Section, we motivate the ansatz Eq. (S22), derive explicit expressions for the scaling functions, and provide details of our fitting procedure for the X^{xz} susceptibility. The discussion for other susceptibilities showing a plateau and scaling in the NFL region (e.g., the current susceptibility $\chi[j_i^a]$) is analogous.

Our scaling ansatz starts from the assumption that the “greater” correlation function of the staggered spin X^{xz} ,

$$\chi_{>}[X^{xz}](t) = -i\theta(t)\langle X^{xz}(t)X^{xz} \rangle, \quad (\text{S26})$$

can be well mimicked by a function $\tilde{\chi}_{>}(t)$ constructed as a superposition of coherent excitations,

$$\tilde{\chi}_{>}(t) = -i\theta(t) \int_T^{T_{\text{NFL}}} d\epsilon \left(\frac{\epsilon}{T}\right)^\nu e^{-i(a\epsilon - ibT)t}. \quad (\text{S27})$$

These coherent excitations have mean energy $a\epsilon$, decay rate bT , and a power-law density of states with exponent ν . We assume that the spectrum of this ansatz,

$$\begin{aligned} \tilde{\chi}_{>}(\omega) &= -i \int_0^\infty dt \tilde{\chi}_{>}(t) e^{i\omega t}, \\ \tilde{\chi}_{>}''(\omega) &= -\frac{1}{\pi} \text{Im} \tilde{\chi}_{>}(\omega), \end{aligned} \quad (\text{S28})$$

captures the low-frequency behavior, $|\omega| < T_{\text{NFL}}$. High frequencies $|\omega| > T_{\text{NFL}}$ are not governed by the quantum critical point and contain information on the local-moment behavior which is not of interest here. The spectrum should also fulfill the fluctuation-dissipation theorem,

$$\tilde{\chi}_{>}''(-\omega) = -\frac{1 - e^{-\omega/T}}{1 - e^{\omega/T}} \tilde{\chi}_{>}''(\omega), \quad (\text{S29})$$

which mainly affects and constrains the very low-frequency spectrum, $|\omega| \lesssim T$. We therefore use our ansatz (S26)

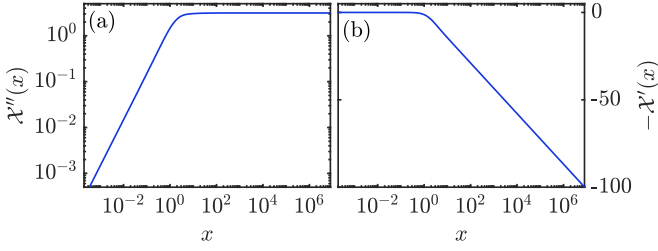


FIG. S7. (a) Spectral part $\mathcal{X}''(x)$ and (b) real part $\mathcal{X}'(x)$ of the scaling function \mathcal{X} , for parameters $\chi_0 = 1, a = 0.1, b = 1$ and $\nu = 0$.

to compute the $\omega > 0$ part of the spectrum (S28) and we then determine the $\omega < 0$ part via Eq. (S29), i.e., we enforce Eq. (S29).

The spectrum of the corresponding retarded correlator is given by

$$\tilde{\chi}''(\omega) = (1 - e^{-\omega/T})\tilde{\chi}''_{>}(\omega), \quad (\text{S30})$$

leading to the ansatz (S22) for $\omega > 0$. The negative-frequency contribution $\tilde{\chi}''(\omega < 0)$ and the real part $\tilde{\chi}'(\omega)$ are obtained via Eqs. (S23) and (S24).

To get the scaling function \mathcal{X}'' , we take the limit of $T_{\text{NFL}} \rightarrow \infty$ in Eq. (S22). (This limit exists for $\nu < 1$, while our data shows $\nu \simeq 0$.) Equation (S22) is then a function of $x = \omega/T$,

$$\mathcal{X}''(x) = \chi_0 \int_1^\infty \frac{dy}{\pi} \frac{(1 - e^{-x})y^\nu b}{(x - ay)^2 + b^2}, \quad x > 0, \quad (\text{S31})$$

$$\mathcal{X}''(-x) = -\mathcal{X}''(x).$$

In Eq. (S24), $\tilde{\chi}'(\omega)$ is singular in $T_{\text{NFL}}/T \rightarrow \infty$ if $\nu \geq 0$. Therefore, we split the real part into a potentially singular static part, $\tilde{\chi}'(0)$, and a non-singular part, $\tilde{\chi}'(\omega) - \tilde{\chi}'(0)$. Using

$$\frac{1}{\omega - \omega'} - \frac{1}{-\omega'} = \frac{\omega}{(\omega - \omega')\omega'},$$

we can take the $T_{\text{NFL}}/T \rightarrow \infty$ limit of the non-singular $\tilde{\chi}'(\omega) - \tilde{\chi}'(0)$ part,

$$\mathcal{X}'(x) = \mathcal{P} \int_{-\infty}^\infty dx' \frac{x\mathcal{X}''(x')}{(x - x')x'}. \quad (\text{S32})$$

This defines the scaling function $\mathcal{X}(x) = \mathcal{X}'(x) - i\pi\mathcal{X}''(x)$. (Note that unlike $\tilde{\chi}'$ and $\tilde{\chi}''$, the scaling functions \mathcal{X}' and \mathcal{X}'' are *not* Kramers-Kronig related.) The asymptotic behavior of the scaling function is

$$\mathcal{X}'(x) \sim \begin{cases} x^2, & |x| \ll 1, \\ (|x|^\nu - 1)/\nu, & |x| \gg 1, \end{cases} \quad (\text{S33a})$$

$$\mathcal{X}''(x) \sim \begin{cases} x, & |x| \ll 1, \\ \text{sign}(x)|x|^\nu, & |x| \gg 1. \end{cases} \quad (\text{S33b})$$

Figure S7 shows $\mathcal{X}(x)$ for the parameters $\chi_0 = 1, a = 0.1, b = 1$ and $\nu = 0$.

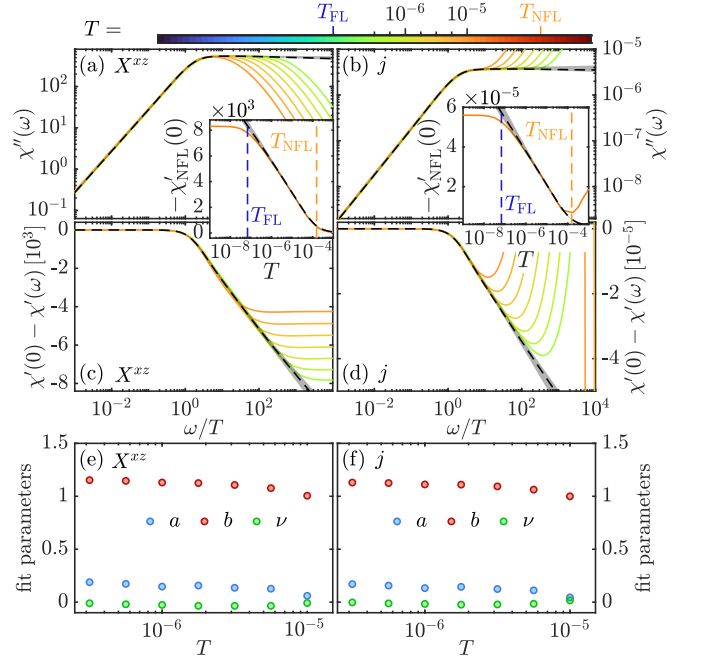


FIG. S8. (a) $\chi''[X^{xz}](\omega)$ and (b) $\chi''[j](\omega)$ (solid lines) versus scaling function $\mathcal{X}''(x)$ (black dashed line). The grey shaded area indicates the deviation when fitting at different temperatures. Only curves used in the fitting process are shown, the ticks on the color bar at the top indicate the temperature, and the color range is the same as in Fig. 2 of the main text. (c,d) Corresponding real parts. Insets: NFL contribution to the static susceptibility. (e,f) Fit parameters at different temperatures. The 95% confidence interval is smaller than the symbol size.

For the potentially singular static contribution $\tilde{\chi}'(0)$, we cannot safely take the $T_{\text{NFL}} \rightarrow \infty$ limit. In the $T_{\text{NFL}}/T \gg 1$ limit, the spectral part $\tilde{\chi}''(\omega)$ sharply drops to zero for $|\omega| > T_{\text{NFL}}$, so that we can approximate $\tilde{\chi}'(0) \simeq \mathcal{X}'_0(T/T_{\text{NFL}})$, with

$$\mathcal{X}'_0(y) = -\mathcal{P} \int_{-y}^y dx' \frac{\mathcal{X}''(x')}{x'}. \quad (\text{S34})$$

$\mathcal{X}'_0(T)$ describes the contribution of the excitations within the NFL region to the static response,

$$\chi'_{\text{NFL}}(0) = -\mathcal{P} \int_{-T_{\text{NFL}}}^{T_{\text{NFL}}} d\omega' \frac{\mathcal{X}''(\omega')}{\omega'}. \quad (\text{S35})$$

The remaining contribution from high-energy excitations,

$$\chi'_{\text{high}}(0) = \chi'(0) - \chi'_{\text{NFL}}(0), \quad (\text{S36})$$

may dominate the temperature dependence of $\chi'(0)$. In that case, $\mathcal{X}'_0(T/T_{\text{NFL}})$ only governs $\chi'_{\text{NFL}}(0)$ but *not* $\chi'(0)$. This is for instance the case for the static current susceptibility, where only $\chi'_{\text{NFL}}[j](0)$ follows $\mathcal{X}'_0(T)$. On the other hand, $\chi'[X^{xz}](0)$ is well described by $\mathcal{X}'_0(T)$ up to an additive constant.

We determine the parameters a, b, ν and χ_0 in Eq. (S31) by fitting logarithms of $\chi''_{>}(\omega)$ to the logarithm of our

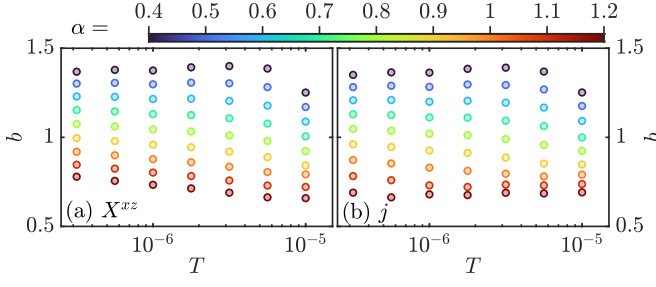


FIG. S9. Effect of log-Gaussian broadening width $\sigma = \alpha \ln \Lambda$ on the fit parameter b for (a) $\chi''[X^{xz}](\omega)$ and (b) $\chi''[j](\omega)$.

scaling ansatz (S31). We employ a least-square fit on a logarithmic frequency grid with 20 grid points per decade and frequencies between $\omega_{\min} = 10^{-9}$ and $\omega_{\max} = T_{\text{NFL}}/4$, i.e., we stay well below the crossover temperature T_{NFL} . Our fits are done for seven logarithmically spaced temperatures between $(T_{\text{FL}} \ll) 10^{-6.5}$ and $10^{-5} (\ll T_{\text{NFL}})$, i.e., for temperatures well separated from the crossover temperatures T_{FL} and T_{NFL} . We then determine a scaling curve by the geometric average over the fitted curves at different temperatures. The largest deviations from the geometric average serve as an error bar. $\mathcal{X}'(x)$ and $\mathcal{X}'_0(T)$ are determined via Eqs. (S32) and (S34), respectively.

Figure S8(a-d) shows the fitting result for $\chi''[X^{xz}](\omega)$ and $\chi''[j](\omega)$. In both cases, our ansatz fits our data very well, with all temperatures yielding very similar curves (the grey area, indicating the largest deviations from the geometric mean, is relatively small). Fig. S8(e,f) shows the results for the fit parameters a , b and ν . The fitting parameters for both $\chi''[X^{xz}](\omega)$ and $\chi''[j](\omega)$ are very similar and the variation with temperature is small. We note that the fits for the highest temperatures are a little less reliable because the plateau in $\chi''(\omega)$ is not that well developed yet. Most important to us is the result for b , which varies between 1.153 at $T = 10^{-6.5}$ and 1.005 at $T = 10^{-5}$ for $\chi''[X^{xz}](\omega)$ and between 1.130 at $T = 10^{-6.5}$ and 0.999 at $T = 10^{-5}$ for $\chi''[j](\omega)$. Thus, our results are consistent with Planckian dissipation, i.e., the lifetime of X^{xz} or current excitations is $\tau \simeq 1/T$, up to a prefactor close to 1.

The fit parameters also depend on how the discrete spectral data from NRG is broadened. For our scaling analysis, we used both a log-Gaussian broadening kernel (cf. Eq. (17) of Ref. [70]) with width $\sigma = 0.7 \ln \Lambda$ ($\Lambda = 3$) and the derivative of the Fermi-Dirac distribution with width $\gamma = T/10$ (cf. Eq. (21) of Ref. [70]) as linear broadening kernel. The broadening parameters are chosen such that the data is almost underbroadened (i.e., discretization artifacts become visible for smaller broadening width). In Fig. S9, we show the effect on b of varying the width $\sigma = \alpha \ln \Lambda$ of the log-Gaussian broadening kernel. Most importantly, b remains of order 1 and changes from $b \simeq 1.4$ for $\alpha = 0.4$ (underbroadened) to $b \simeq 0.66$ for $\alpha = 1.2$ (overbroadened). Interestingly, the parameter b which determines the decay rate *decreases* with *increasing*

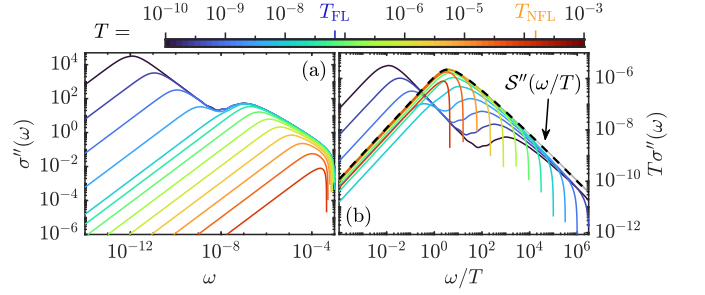


FIG. S10. (a) Imaginary part of the optical conductivity at different temperatures. $\sigma''(\omega)$ becomes negative around $\omega \gtrsim 10^{-3}$. (b) Dynamical scaling of the imaginary part. In the NFL region, all curves fall onto the scaling curve $\mathcal{S}''(\omega/T)$. Data at $\omega > 10^{-3}$ has been omitted for clarity.

broadening width. The linear broadening parameter γ (not shown) appears to have the converse effect, i.e., lower γ leads to lower b and vice versa.

S-V. COMPLEX OPTICAL CONDUCTIVITY

The scaling behavior of the current susceptibility in the NFL region implies a related scaling behavior for the complex optical conductivity $\sigma = \sigma' + i\sigma''$. The scaling of its real part, $T\sigma'(\omega, T) = (T/\omega)\pi\mathcal{X}''(\omega/T) = \mathcal{S}'(\omega/T)$, is discussed in the main text. The imaginary part is obtained via a Kramers-Kronig relation from the real part,

$$T\sigma''(\omega, T) = \mathcal{P} \int \frac{d\omega'}{\pi} \frac{T\sigma'(\omega', T)}{\omega - \omega'} = \frac{T}{\omega} \mathcal{X}'(\omega/T), \quad (\text{S37})$$

where for the last step, we evoked Eq. (S32). It is thus likewise expected to show scaling behavior in the NFL region. Indeed it does, as shown in Fig. S10.

To summarize, the scaling behavior of $\sigma(\omega, T)$ can be expressed through the scaling function $\mathcal{X}(x)$ governing the current susceptibility, as follows:

$$T\sigma(\omega, T) = \mathcal{S}(x) = -\frac{1}{ix} \mathcal{X}(x) = \mathcal{S}'(x) + i\mathcal{S}''(x),$$

$$\mathcal{S}'(x) = \frac{\pi}{x} \mathcal{X}''(x), \quad \mathcal{S}''(x) = \frac{1}{x} \mathcal{X}'(x). \quad (\text{S38})$$

The asymptotic behavior of $\mathcal{S}(x)$ follows from Eqs. (S33b) and (S33a),

$$\mathcal{S}'(x) \sim \begin{cases} \text{const.}, & |x| \ll 1, \\ |x|^{\nu-1}, & |x| \gg 1, \end{cases} \quad (\text{S39a})$$

$$\mathcal{S}''(x) \sim \begin{cases} x, & |x| \ll 1, \\ (|x|^\nu - 1)/\nu x, & |x| \gg 1. \end{cases} \quad (\text{S39b})$$

The ω/T scaling of the optical conductivity implies ω/T scaling of the dynamical transport scattering rate and of the effective mass,

$$\tau^{-1}(\omega, T)/T = \text{Re}[T\sigma(\omega, T)]^{-1},$$

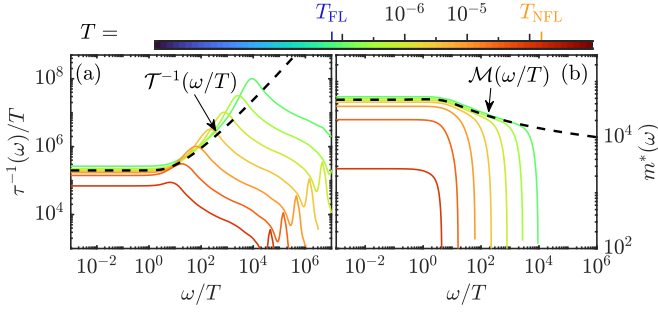


FIG. S11. (a) Scaling of the dynamical scattering rate $\tau^{-1}(\omega)$ and (b) of the optical mass $m^*(\omega)$ in the NFL region. The dashed lines denote the scaling functions $\mathcal{T}^{-1}(\omega/T)$ and $\mathcal{M}(\omega/T)$, respectively.

$$= \text{Re} [\mathcal{S}(\omega/T)]^{-1} = \mathcal{T}^{-1}(\omega/T) \quad (\text{S40})$$

$$\begin{aligned} m^*(\omega, T) &= -\frac{T}{\omega} \text{Im} [T\sigma(\omega, T)]^{-1} \\ &= -\frac{T}{\omega} \text{Im} [\mathcal{S}(\omega/T)]^{-1} = \mathcal{M}(\omega/T). \end{aligned} \quad (\text{S41})$$

In the main text, we have shown that $\tau^{-1}(\omega, T) = \tau_0^{-1} + c(T)\omega^2$ at low frequencies in the scaling region. The ω/T scaling above then implies $\tau_0^{-1} \propto T$ and $c(T) \propto 1/T$.

Figure S11 shows the ω/T scaling of both $\tau^{-1}(\omega)$ and $m^*(\omega)$. Both follow their respective scaling curves well within the NFL region, i.e., for $T_{\text{FL}} \ll T \ll T_{\text{NFL}}$ and $\omega/T \ll T_{\text{NFL}}/T$ (for $T = 10^{-7}$, the lowest temperature shown, $T_{\text{NFL}}/T \simeq 1.5 \times 10^3$).

S-VI. CHOICE OF MODEL PARAMETERS: COMPARISON TO EXPERIMENT

In this section, we give a crude estimate on how our model parameters compare to expectations for CeCoIn₅. Our goal is to provide some background on our comparison in Fig. 4 of the main text. The first thing to stress is, however, that our PAM is a toy model that cannot be expected to precisely describe the physics of real heavy-fermion materials over a broad range of energy scales. These systems have multiple bands, multiple Fermi surfaces, and 14-fold degenerate f levels instead of the two-fold degenerate f levels used in our PAM. However, at sufficiently low energies, we believe that our model is sufficiently accurate for two reasons: First, critical phenomena are universal and are insensitive to the details when one focuses on low-energy phenomena. Second, the f orbitals in both the 115 materials and YbRh₂Si₂ are subject to tetragonal crystal fields such that a single Kramers doublet is active at low energies, justifying our description by the effective two-fold degenerate f levels [96].

Specifically for CeCoIn₅, the low-energy $j = 5/2$ multiplet is split into three Kramers doublets, denoted Γ_7^- , Γ_7^+ , and Γ_6 [96]. Of those, Γ_7^- has the lowest energy; Γ_7^+ has an excitation energy of $E_7^+ \simeq 6.8 \text{ meV} = 79 \text{ K}$ while the excitation energy of Γ_6 is $E_6 \simeq 25 \text{ meV} = 290 \text{ K}$. The

coherence scale (T_{NFL} in our manuscript) of CeCoIn₅ is 40 K [112] and therefore clearly lower than E_7^+ . Therefore, it seems reasonable to describe the universal physics in the vicinity or below the coherence scale in terms of a single orbital (modeling the Γ_7^- doublet). However, the Γ_7^+ doublet could play a role in establishing the value of the coherence scale, T_{NFL} , as we will elaborate below.

Let us now outline why we believe that for our toy PAM our choice of parameters (adopted from prior 2CDMFT studies [56, 63, 64]) is reasonable, at least in order of magnitude. In our NRG computations we take the half-bandwidth, say W , as an energy unit, i.e., we set $W = 1$. The half-bandwidth is a very high energy scale, not directly relevant for the low-energy physics. If, for argument's sake, we take the full bandwidth $D = 2W$ to be 1 eV, ($W \sim 0.5 \text{ eV}$) [97, 98], then the parameter choices made in our paper imply $U = 10W = 5 \text{ eV}$, which is the usual order-of-magnitude value for Ce compounds [99, 100], and $-\epsilon_f = 5.5W = 2.75 \text{ eV}$, somewhat similar to the value 2 eV observed in the photoemission spectrum of Ce compounds [99].

Finally, our choice of $V = 0.46W = 0.23 \text{ eV}$ for the impurity-bath hybridization V in the Anderson model implies an effective exchange coupling, $J_{\mathbf{K}} \mathbf{S}_{\text{imp}} \cdot \sum_{\mathbf{k}, \mathbf{k}', s, s'} \psi_{\mathbf{k}s}^\dagger \sigma_{ss'} \psi_{\mathbf{k}'s'}$, of strength [cf. Eq. (1.73) of Ref. [101]]

$$J_{\mathbf{K}} = V^2 \left(\frac{1}{\epsilon_f} + \frac{1}{\epsilon_f + U} \right) \simeq 0.043 \text{ eV}. \quad (\text{S42})$$

This quantity determines the coherence scale (called T_{NFL} in our work), which for the one-band Anderson model is roughly given by [cf. Eq. (3.47) of Ref. [101]]

$$T_{\text{NFL}}/W \simeq \sqrt{2J_{\mathbf{K}}\rho} \exp\left(-\frac{1}{2J_{\mathbf{K}}\rho}\right). \quad (\text{S43})$$

Here, ρ is the density of states per spin at the Fermi level. For a featureless band, one would have $\rho = 1/2W = 1/\text{eV}$. However, in the more realistic case (and also for the periodic Anderson model) ρ is not featureless, hence the value for ρ entering the formula for T_{NFL} is more of an effective parameter. Indeed, our 2CDMFT calculation using the above choice of bare parameters leads to a coherence scale of $T_{\text{NFL}} \simeq 1.55 \times 10^{-4} W$. According to Eq. (S43), this corresponds to $J_{\mathbf{K}}\rho \simeq 0.065$. With $J_{\mathbf{K}} \simeq 0.043 \text{ eV}$ [from Eq. (S42)] we get $\rho \simeq 1.51/\text{eV}$, quite a bit larger than the $\rho = 1/\text{eV}$ obtained for a featureless band.

For CeCoIn₅, we assume that the coherence scale is influenced by the presence of the Γ_7^+ doublet. We take that into account by means of an effective orbital degeneracy N^{CCI} , which is a free parameter that is expected to be larger than 1, but not (significantly) larger than 2 since we expect the Γ_6 excitation to play a negligible role. To estimate the coherence scale, we use the position of the resistivity maximum, $T_{\text{NFL}}^{\text{CCI}} \simeq 40 \text{ K} = 0.0034 \text{ eV}$ [112] (in

the PAM, the resistivity maximum is slightly below T_{NFL} , though this does not matter for an order-of-magnitude estimate). For an N -orbital Anderson model, the Kondo temperature and effective exchange coupling are related by [cf. Eq. (D.18) of Ref. [101]]

$$T_{\text{NFL}}/W \simeq (2NJ_K\rho)^{1/2N} \exp\left(-\frac{1}{2NJ_K\rho}\right). \quad (\text{S44})$$

Using the same “effective impurity model” parameters of $(J_K, W) \simeq (0.043, 0.5)$ eV and $\rho \simeq 1.51/\text{eV}$ estimated from our PAM result, we find that a value of $T_{\text{NFL}}^{\text{CCI}} \simeq 0.0034$ eV is obtained for an effective orbital number of $N^{\text{CCI}} \simeq$

1.5. This suggests that apart from Γ_7^- , the Γ_7^+ crystal field excitation indeed does play a role in establishing the coherence scale. At even lower energies, the Γ_7^+ excitation presumably freezes out hence a one-orbital description of the low-energy physics seems reasonable.

All in all, our parameter choice for the PAM seems to be suitable for a rough description of CeCoIn₅. That said, the above arguments are clearly very heuristic. A quantitative analysis beyond the universal phenomena will require a more elaborate study using a more realistic model (treated using LDA+DMFT+NRG).